

Interpretable Machine Learning for Urban Heat Mitigation: Attribution and Weighting of Multi-Scale Drivers

David Immanuel TSCHAN^{1,2}; Zhi WANG¹; Jan CARMELIET¹; Yongling ZHAO^{1,*}

¹ Department of Mechanical and Process Engineering, ETH Zürich, Switzerland

² Department of Environmental Systems Science, ETH Zürich, Switzerland

* Correspondence to: vozhao@ethz.ch

Abstract

Urban heat islands (UHIs) are often accentuated during heat waves (HWs) and pose a public health risk. Mitigating UHIs requires urban planners to first estimate how urban heat is influenced by different land use types (LUTs) and drivers across scales — from synoptic-scale climatic background processes to small-scale urban- and scale-bridging features. This study proposes to classify these drivers into driving (D), urban (U), and local (L) features, respectively. To increase interpretability and enhance computation efficiency, a LUT-distinguishing machine learning approach is proposed as a fast emulator for Weather Research and Forecasting model coupled to a Single-Layer Urban Canopy Model (WRF-SLUCM) to predict ground- (TSK) and 2-meter air temperature (T2). Using random forests (RFs) with extreme gradient boosting (XGB) trained on WRF-SLUCM output over Zurich, Switzerland, during heatwave (HW) periods in 2017 and 2019, this study proposes LUT-based (LB) models that categorize features by scales and practical controllability, allowing optional categorical weighting. This approach enables category-specific feature ranking and sensitivity estimation of T2 and TSK to most important small-scale drivers — most notably surface emissivity, albedo, and leaf area index (LAI). Models employing the LB framework are statistically significantly more accurate than models that do not, with higher performance when more HW data is included in training. With RF-XGB robustly performing optimal with unit weights, the method substantially increase interpretability. Despite the needs to reduce statistical uncertainties and testing the method on other cities, the proposed approach offers urban planners a direct framework for feasibility-centered UHI mitigation assessment.

Plain Language Summary

Urban heat islands (UHIs) have major consequences for human health, especially during heat waves (HWs). To reduce temperatures in cities, knowing which features may lead to the highest temperature increases is important. Often, the Weather Research and Forecasting (WRF) model coupled to a single-layer urban canopy model (SLUCM) has been used for this. This study proposes a method to increase speed and interpretability of feature importance estimates. For this, random forests (RFs) and extreme gradient boosting (XGB) are used to emulate WRF-SLUCM to predict ground- and 2m temperature (TSK, T2) over Zurich, Switzerland, for HW periods in 2017 and 2019. Before fitting, features are grouped into categories pertaining to different scales at which parameters influence UHIs, and categories may be weighted. Features within each category are then ranked and the most important features from the small-scale category are used to estimate mitigation potentials. Models using this method perform better than if the method is not applied, and predictions become more accurate if more HW data is used to train RFR-XGB. The method robustly indicated optimal weights of unity, and successfully identifies the most important small-scale drivers as emissivity, albedo and leaf-area index (LAI). More work is required to decrease statistical uncertainties and demonstrate the method for other cities. Nevertheless, this study shows that the method produces highly interpretable and meaningful results, and that it offers a tool that urban planners can use to create UHI mitigation strategies with high feasibility.

1 Introduction

Urban areas (UAs) characterized by higher air- and surface temperatures compared to surrounding rural areas are often called urban heat islands (UHIs) (Oke, 1982). Specific configurations in UAs lead to microclimates with surface temperature (TSK) and 2m-temperature (T2) up to 4 – 11 °C (Hassan et al., 2021; Keith et al., 2023; Varentsov et al., 2018) and 7.8 °C (Phelan et al., 2015), respectively, warmer than in rural surroundings, driven through altered energy and humidity exchange (Chen et al., 2014). Larger UAs associated with larger impermeable surfaces increase TSK (Hua et al., 2020) and tend to aggravate UHIs-caused heat stress (Ren et al., 2023; Wang, 2023), particularly during heat wave (HW) events (Ward et al., 2016) that enhance nighttime urban heating (Kong et al., 2023). These may increase in the future (Intergovernmental Panel On Climate Change (IPCC), 2023). Associated heat exposure effects include elevated energy consumption and water demand, deteriorating air quality and human health risks (Boned Fustel et al., 2021; Ebi et al., 2021; Ward et al., 2016) especially for groups at risk (Li and Bou-Zeid, 2013; *Verein Klimaseniorinnen Schweiz and Others v. Switzerland*, 2024; Yang et al., 2021). With UAs likely to grow and host larger shares of populations (United Nations Organisation, 2019), UHIs are a major effect of climate change and urbanisation and pose an increasing public health risk.

Minimising UHI impacts requires implementation of mitigation strategies. To inform such strategies for large-scale implementations, numerical weather prediction (NWP) systems have proven effective in assessing UHI drivers. Frequently, the Weather Research and Forecasting (WRF) model (Skamarock et al., 2021) is employed, demonstrating good performance under heatwave (HW)- and non-heatwave (NHW) conditions (Chen et al., 2014; Giannaros et al., 2018; Li et al., 2019), often used in conjunction with single-layer or multi-layer urban canopy models (UCMs). WRF-simulations may be used to assess strategies such as increased urban vegetation and roof cooling (Cui and Foy, 2012; Li and Norford, 2016). They may also highlight major UHI drivers across scales, such as meso- or synoptic-scale

atmospheric circulation (Aquino-Martínez et al., 2025), urban scale surface albedo and emissivity configurations (Giannaros et al., 2018), urban anthropogenic heat release (Chen et al., 2014), or scale-bridging parameters such as nighttime urban boundary layer structure (Cui and Foy, 2012). These studies also indicate that UHIs may vary with terrestrial morphology, such as proximity to oceans and elevation (Vahmani and Ban-Weiss, 2016), background climate (Zhao et al., 2014), and urban land-use types (LUTs) (Chen et al., 2014; Li and Norford, 2016). Consequently, with drivers varying across scales, mitigation strategies based on driver characterization are expected to have different effects in different cities (Georgescu et al., 2014).

These findings emphasise the need to design city-specific UHI mitigation strategies that account for processes across all scales and LUT-induced UHI variations. Importantly, different drivers belonging to different scales may exhibit different degrees of modifiability. This, along with the fact that different LUTs may be associated with different drivers, may lead to difficulties for urban planners to (1) assess which scales are most important for their UAs; (2) determine which features to choose for adaptation measures out of the pool of modifiable features within their UAs; and (3) estimate the resulting mitigation potential given the scale at which the chosen features affect UHIs. Despite growing understanding of UHIs, urban planners face a lack of effective methodology to address these questions for their respective cities (Carmeliet and Derome, 2024).

To alleviate this issue, NWP-UCM schemes provide a viable tool. However, despite recent advances, NWP applications for UHI research remain challenging and computationally expensive (Andraju et al., 2019; Chen et al., 2014; Lean et al., 2024; Wang et al., 2019; Zhong et al., 2023). For mitigation assessment, supervised machine learning (ML) is an attractive alternative to fully or partially emulate NWP-UCM schemes, delivering fast estimators for mitigation potentials. A promising method is random forest (RF) regression employing extreme gradient boosting (RFR-XGB). It is efficient with large

datasets, requires limited hyperparameter (HP) tuning and offers high interpretability. RFR-XGB has been used to identify seasonal differences in UHI drivers (Liu et al., 2023) and to suggest urban greening and permeable surfaces as UHI mitigation strategies (Mohammad et al., 2022). The results of well-calibrated RFR-XGB models are largely in line with NWP-UCM scheme predictions, and they may therefore provide viable alternatives to NWP-based systems. RFR-XGB has also enabled measurement of the impact of different indices related to water and vegetation in UAs on UHIs (Garzón et al., 2021), and has been used to assess the importance of different LUTs on urban area land surface temperatures (McCarty et al., 2021). These are important steps towards assessing importance of urban climate drivers to inform pertaining mitigation potentials in a computationally efficient way. Nevertheless, these results are constrained to particular cities or regions and offer limited generalisability into a universal framework.

This study aims to close that gap by first introducing a machine learning (ML) method tailored for UHI mitigation. In addition, it proposes, examines, and demonstrates the critical important of ranking and selecting features with a similar degree of modifiability for UHI mitigation — both when distinguishing LUTs in the model and when not, with such distinguishing accounting for the different physical regimes in surface energy balance across LUTs found in various studies (Chen et al., 2014; Li and Norford, 2016). It is assumed that small-scale drivers are generally easily modifiable, whereas larger scale drivers are hardly or not modifiable, which allows focusing on relevant, modifiable drivers for mitigation potential assessment. To this end, prior to ranking and selecting optimal feature sets, features are pooled into categories that impact UHIs on similar scales and exhibit similar degrees of controllability by urban planners. Then, optimal feature sets are subjected to differential weighting across categories to determine the relative impact of different scales on UHIs. To obtain feature importances and mitigation potentials, RFR-XGB regression is used to emulate the WRF model coupled to a single-layer UCM to predict surface- and 2m-air temperatures (TSK, T2), respectively.

Specifically, the aims of the study are (1) to show that HW data is required in the training data set to reproduce HW conditions in predictions; (2) to demonstrate that LUT-specific land-based (LB) models increase performance compared to city-based (CB) models that do not distinguish LUTs; and (3) to show that LB models applying the proposed method — feature preclassification, subsequent feature set optimization, and weighing of features across categories — maximise both interpretability and performance. This is demonstrated for Zurich, Switzerland, where a significant UHI has been reported (Canton and Dipankar, 2024). While the demonstration is limited to a single urban area, the approach is designed to be generalisable and can be readily extended to urban heat mitigation studies in cities with diverse local contexts. To the best of the authors' knowledge, this is the first study that provides decision-makers and urban planners with a scalable method to assess the dominant UHI-driving scale in their urban area, to select the most relevant modifiable features for mitigation, and quantify the associated mitigation potentials.

2 Method

2.1 Overview

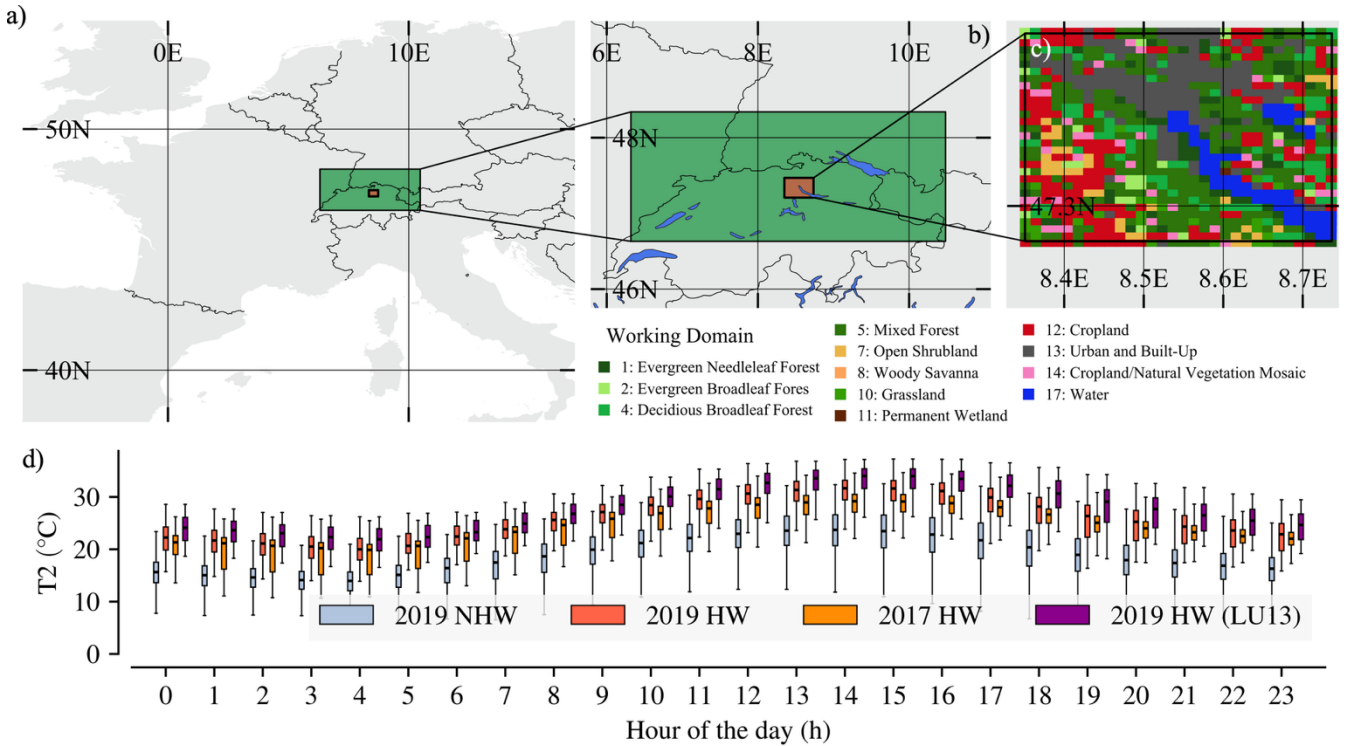


Figure 1: a: Overview over domains within Europe. b: WRF-SLUCM domain (green) and working domain (WD) (red) over Switzerland. c: Detailed view of WD over Zurich, Switzerland. d: Diurnal cycle of T2 for the WD for different data sets. There is a clear distinction in the diurnal cycle for HW and NHW conditions, with climatological temperature in highest during HW for LUT 13. Indicated are median temperatures, while bars extend to 25th and 75th percentiles, respectively. Shown values pertain to WD without LUT 17 (water).

This study uses output from WRF coupled to a single-layer urban canopy model (SLUCM) to train a RFR-XGB emulator for T2 and TSK. Spatial data extent is 309km west-east and 189km south-north over middle Europe (fig. 1a). From this, a subspace spanning 30km × 30km over the region of Zurich, Switzerland (fig. 1c) is selected as the study working domain (WD). Temporally, data covers two periods, July 2017 including only HW data, and June and July 2019 containing both HW and NHW data. HW data has higher T2 over the diurnal cycle than NHW data (cf. fig. 1d), especially pronounced for LUT 13 (urban and built-up). The WRF-SLUCM data contains 24 variables (cf. table 3, supplementary materials), with T2 and TSK used as targets and all others as features, and 12 different LUTs. Data with

LUT representing water was removed for both CB- and LB- models because water areas follow different energy balance regimes than terrestrial LUTs.

2.2 City-Based Models and Land-Based Models

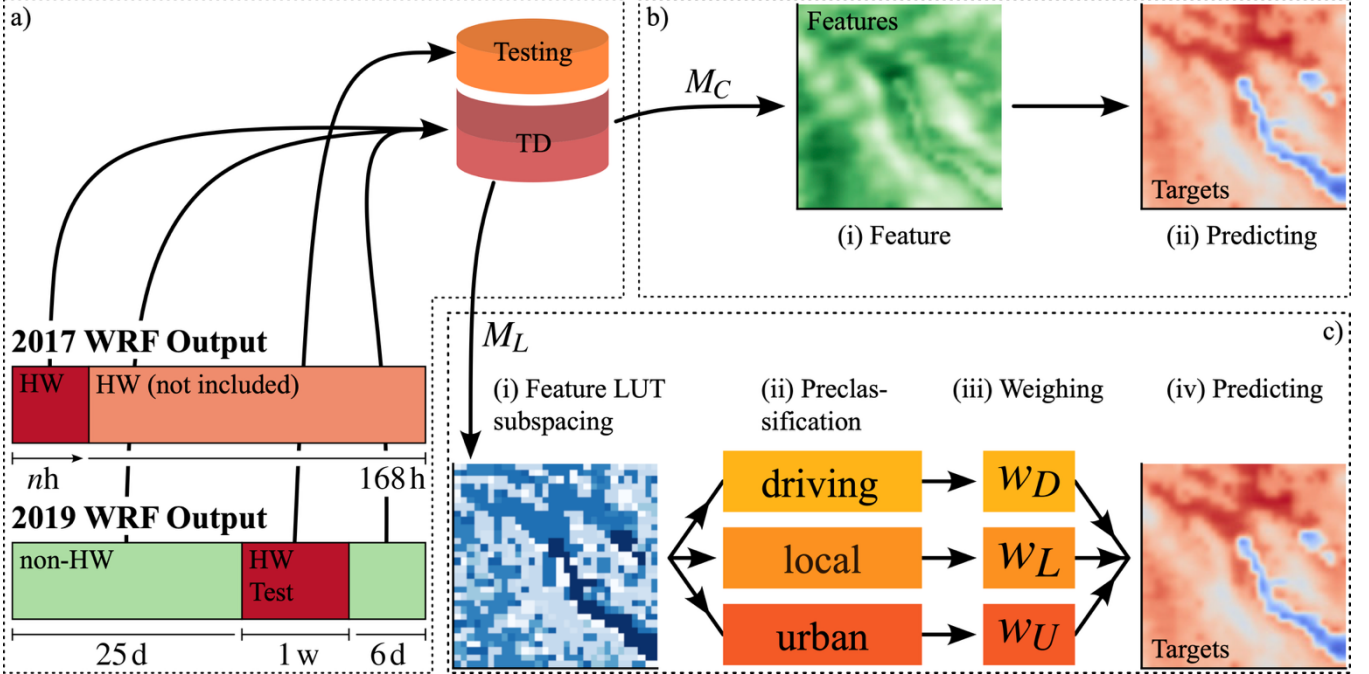


Figure 2: a: Aggregation of data into a dataset. 2017 heat wave (HW) data and 2019 non-heat wave (NHW) data is aggregated into the training data (TD), while the test data consists of 2019 HW data. b: City-based (CB) model M_C . In such models, features from the dataset (step i) are directly used to train RFR-XGB to predict T2 and TSK (step ii). c: Land-based (LB) model M_L . In such models, the feature space is first split into LUT subspaces (step i). The features are then preclassified into driving (D)-, local (L) and urban (U)-features that pertain to synoptic-scale-, scale-bridging- and urban-scale processes (step ii). The features in each group are then subjected to weighting multiplying all features from each category with the pertaining weight w_D , w_L , w_U (step iii). Finally, an CB model is trained on this LUT-specific data to predict T2 and TSK for the pertaining LUT (step iv). The complete LB model consists of the aggregated CB models, each pertaining to a specific LUT.

2.2.1 City-Based Models

For city-based (CB) models, data is aggregated from WRF-SLUCM output (fig. 2a). All 2019 NHW data as well as variable number of 2017 HW data hours are included in the training set, and the testing set consists of all 2019 HW data. CB models (fig. 2b) do not distinguish LUTs. Instead, a CB model including n_t features, denoted $M_C^{(n_t)}$, learns the relationship of features — independently of the scale

they pertain to or their degree of modifiability in a mitigation setting (fig. 2bi) — and T2 and TSK and predicts estimates of these targets (fig. 2bii).

2.2.2 Land-Based Models

For land-based (LB) models, data is aggregated similarly to CB models (fig. 2a). Unlike CB models, however, LB models (fig. 2c) distinguish LUTs to account for different physical energy balance regimes, classify features into driving (D)-, local (L) and urban (U) features — pertaining to meso- to synoptic scales, scale-bridging scales and small urban scales — and assign weights to them.

Classification accounts for different underlying scales and associated differences in modifiability, while weighting represents the differential influence of scales on UHIs. Concretely, a LB model containing n_D (D)-, n_L (L)- and n_U (U)-features, denoted $M_L^{(n_D, n_L, n_U)}$, splits the feature space into LUT specific subspaces (fig. 2ci) and fits CB submodels on each LUT subspace, such that the LB models consists of the totality of CB submodels. After LUT-splitting, features are pre-classified into categories (fig. 2cii) and each category may be weighted with weights w_D , w_L , w_U to represent the differential importance of D-, L- and U-scales (fig. 2ciii). The model $M_L^{(n_D, n_L, n_U)}$ then learns the relationship between features and targets and predicts an estimate of T2 and TSK (fig. 2civ). To obtain TSK and T2 predictions across the entire WD, the estimates must be gathered across LUT-specific submodels.

2.3 Data, Preprocessing and Feature Categorization

2.3.1 Data

The WRF-SLUCM data used to train CB- and LB models has spatial resolution of $1km$ and temporal resolution of $1h$. HW data for 2017 spans the period between 18.06.2017 and 24.06.2017. NHW data of 2019 spans the period between 01.06.2019 to 08.07.2019, except for a HW event between 25.06.2019 and 02.07.2019. Totally, 2017 data includes $168h$ of HW data, and 2019 data includes 25 days of NHW data followed by 1w of HW data followed by 6 days of NHW data. The training dataset (TD) for RFR-XGB consists of up to 168 variable hourly data slices of 2017 HW data and the entire 2019 NHW data (fig. 2a). The test dataset consists of the week of HW data from 2019.

2.3.2 Preprocessing

During preprocessing, data is scaled and shuffled. Scaling is implemented to assure all features are of similar order of magnitude so that RFR-XGB does not learn on features' absolute magnitudes. Because feature distributions are different (cf. table 3, supplementary material; consider mean and skewness of features), data was scaled using the min-max approach (Tanoori et al., 2024) in which for every feature f , the transformation

$$\tilde{f}_i = \frac{f_i - \downarrow f_j}{\uparrow f_j - \downarrow f_j} = \frac{f_i - \min_j f_j}{\max_j f_j - \min_j f_j} \quad (1)$$

is applied such that transformed features exhibit $\tilde{f}_i \in [0, 1] \forall f$. Importantly, training and testing features must be scaled with the same scaling parameters $\uparrow f_j = \max_j f_j$, $\downarrow f_j = \min_j f_j$, obtained from the TD only. After scaling, data is randomly shuffled to reduce overfitting.

There is a set of categorical features present in the data, including soil type, vegetation type and, for CB models, LUT. Since these are present on an ordinal scale, they were subjected to the same preprocessing steps as numerical features and not treated specially.

2.3.3 Feature Preclassification

As described in the section 2.2.2, features were preclassified into the U- (urban or small-scale), L- (local or scale-bridging), and D-features (driving or meso- to synoptic scale) in LB models. Preclassification thereby accounts for both the assumed scale-modifiability relationship and the notion that feature ranking is most meaningful for mitigation potential assessment if the ranked features are modifiable to the same degree. For example, solar zenith angle or terrain height are driving features, whereas leaf area index (LAI) or vegetation type are urban features. While solar zenith angle and terrain height are not modifiable, LAI or vegetation types in cities are easily modifiable. Low level wind speed is a local

feature, as it is determined both by synoptic-scale atmospheric states and small-scale urban 3D structure. Accordingly, its degree of modifiability is intermediate: altered urban building morphology — an aspect that may be controlled in urban design — may allow for more circulation. However, circulation is subject to large-scale controls through synoptic-scale circulation or proximity to oceans or topography — aspects not controllable in cities. Detailed justification why any given feature belongs in any given category can be found in the supplementary materials (sec. 7.2). Importantly, categorization is dependent on the available data and the UA for which it is applied. From the total of $N_t = 22$ features available for CB models, there are $N_D = 6$ D-, $N_L = 10$ L- and $N_U = 5$ D-features considered in this study, with LUT not considered a feature in MB models.

2.4 Metrics

Predicted targets may be scored against testing data using $R^2 \in (-\infty, 1]$ scores from the true-, predicted- and average target values $y_i, \hat{y}_i, \bar{y}_i$ from the training process:

$$R^2 = 1 - \frac{\sum_i^N (y_i - \hat{y}_i)^2}{\sum_i^N (y_i - \bar{y})^2} \quad (2)$$

This metric increases when more data variance becomes explicable by the model. As two targets were considered in this study, i.e. T2 and TSK, a separate model was fitted for each target and the overall accuracy is the averaged accuracy across the two targets, i.e.

$$R_{\text{avg}}^2 = \frac{1}{2} [R^2(\text{T2}) + R^2(\text{TSK})] \quad (3)$$

2.5 Experimental Workflow

This study uses a sequential methodology:

1. Fitting baseline CB and LB models $M_{C,0}^{(22)}$, $M_{L,0}^{(6,10,5)}$, respectively, that include all features. In this step HPs are tuned using 10-fold cross validation (CV) and all 168h of 2017 HW data. For LB models, this means that the underlying set of CB models is subjected to HP tuning, such that HPs differ across LUTs. Subsequent models use the same hyperparameters as the baseline models, whereas all other parameters — particularly the number of features and HW training hours from 2017 — may be varied.
2. Running a feature ranking scheme based on sequential backward selection (SBS) to obtain feature-inclusion orders (FIOs) (see sec. 2.7) that represent a feature importance ranking. For LB models, FIOs are LUT- and category-specific.
3. Optimizing feature sets — that is finding optimal n_t for CB models and optimal (n_D, n_L, n_U) for LB models — using variable numbers of features from the FIOs. This results in optimised CB and LB models denoted with $M_{C,B}$, $M_{L,B}$, respectively.
4. Applying the resulting optimal models to assess the mitigation potential of the most important features identified in step 3.

2.6 Random Forests and Extreme Gradient Boosting

This study uses RFR-XGB, where XGB is provided via the open-source XGBoost library (Chen and Guestrin, 2016). RFR-XGB may result in RFs with low variance and high predictive power, in a computationally efficient manner that may be fitted on a personal computer. While other ML methods, particularly neural networks, may be well-suited for UHI mitigation research (Wang et al., 2023), associated computational costs and required data quantities may be high. Computational cost of other methods may therefore be high if training is not outsourced to appropriate high-performance infrastructure. Likely, urban planners and decision-makers do not have these resources at their disposal. This is the main factor favouring RFR-XGB in the context of this study.

2.7 Feature Ranking Scheme

Once the baseline CB and LB models ($M_{C,0}$ and $M_{L,0}$) have been established, a feature selection scheme is proposed and implemented. This feature selection scheme is based on sequential backward selection (SBS) (Raschka and Mirjalili, 2019). Contrastingly to regular SBS implementations, this study identifies the feature causing the most — rather than the least — decrease in performance at each iteration and removes it from the feature set. While in CB models, this feature selection scheme is applied to the entire feature set, it needs to be applied for each LUT submodel and for each of the D-, L- and U feature categories separately in LB models. Let $F^{(n)}$ denote the baseline feature set consisting of n features, that is, $F^{(n)} = \{f_1, f_2, \dots, f_n\}$. For CB models, this is a single feature set $F^{(n_t)}$ containing all $n_t = 22$ features while for LB models, there are three baseline feature sets $F^{(n_D)}$, $F^{(n_L)}$, $F^{(n_U)}$ with $n_D = 6$, $n_L = 10$, $n_U = 5$ features, pertaining to D-, L-, and U-features, respectively. For $F^{(n_t)}$, $F^{(n_D)}$, $F^{(n_L)}$ and $F^{(n_U)}$ the feature selection scheme starts at iteration $t = 0$ and recursively creates a list ${}_*F$:

1. Initialise a list ${}_*F$.
2. Using the feature set $F^{(n-t)}$ at iteration t , fit $n - t$ models on the $n - t$ feature subsets $F^{(n-t)} \setminus f_k = \{f_i\}_{i \neq k}^{n-t}$. This results in a set of $n - t$ scores $\{r_i\}_{i=1}^{n-t} = \{R_{\text{avg}}^2(\{f_i\}_{i \neq k})\}_{k=1}^{n-t}$.
3. Determine $1 \leq j \leq n - t$ such that $r_j = \min_k \{r_k\}_{k=1}^{n-t}$, which pertains to feature f_j .
4. Set $F^{(n-[t+1])} = F^{(n-t)} \setminus f_j$.
5. Determine the number of features in $F^{(n-[t+1])}$.
 - a. If $F^{(n-[t+1])}$ contains more than one feature, append f_j to ${}_*F$, set $t \leftarrow t + 1$ and go to 2.
 - b. If $F^{(n-[t+1])}$ contains one feature, append this feature to ${}_*F$ and terminate.

Thus in each iteration, the feature selection scheme removes the feature whose removal causes the *highest* loss in R_{avg}^2 score relative to the removal of all other features, and appends this feature the FIO

*F . After termination ${}^*F = \{ {}^*f_i \}_{i=1}^n$ constitutes a feature set containing the initial number n of features *ordered* — indicated through the subscript $*$ — in descending importance, where for $1 \leq j < n$ the feature *f_j is more important than ${}^*f_{j+1}$. Such an ordered feature set *F is referred to as a feature inclusion order (FIO).

Importantly, FIOs do not result in an absolute importance scale for features. Given the FIO

${}^*F = \{ {}^*f_i \}_{i=1}^n$, claiming that *f_k is more important than *f_j if $j < k \leq n$ holds not *per se*, because *f_k was determined from a feature set from which *f_j has already been removed. Rather, FIOs represent a *hierarchical* importance scale: given the FIO ${}^*F = \{ {}^*f_i \}_{i=1}^n$, for $s < n$, if feature *f_s is included, the next feature to be included should be ${}^*f_{s+1}$ in order to cause the highest increase in variability explicable by the model. Feature importance in this study should be understood in this hierarchical sense.

2.8 Optimal Feature Sets and Weighting of Categories

Through increasing the number of ordered features, FIOs may serve to construct sequential feature sets

$F^{(*m)} = \{ {}^*f_i \}_{i=1}^{*m \leq n}$. By finding $F^{(*k)} = \arg \max_{*m} R_{\text{avg}}^2 \left(F^{(*m)} \right)$, an optimal feature set may be

identified. For CB models, the identified optimal feature set with *n_t features pertains to the entire WD

and allows to find an optimal model $M_{C,B}^{(*n_t)}$, where “ B ” denotes an optimised model.

For LB models, per LUT, three FIOs — pertaining to D-, L- and U-features — are required, to find the optimal numbers of features *n_D , *n_L , *n_U , which may then be aggregated into an optimal model

$M_{L,B}^{(*n_D, *n_L, *n_U)}$. This requires including the same number of features per category across LUTs, even

though the included features per category are different across LUTs. Such models imply unit weight of

all categories and are hence called *non-weighted*, denoted ${}_{nw}M_{L,B}^{(*n_D, *n_L, *n_U)}$.

Contrastingly, weights w_D, w_L, w_U for driving-, local-, and urban- features differing from unity may be assigned to each category, resulting in models referred to as *weighted*, denoted ${}_wM_{L,B}^{(*n_D, *n_L, *n_U)}$.

Importantly, these weights are *not* computed internally by RF-XGB but are *assigned* to the categories to reflect their relative importance, and are hence different from the weights normally associated with random forest regression. In this study, *weights* explicitly refer to these *assigned* weights. Detailed methodology on how to obtain such weights for categories is outlined in the supplementary materials (cf. sec. 7.3).

2.9 Procedure to obtain Optimal Feature Sets

Through sequentially including more features from the FIO, an optimal CB model $M_{C,B}$ may be identified. To find the best non-weighted LB model ${}_{nw}M_{L,B}$, the total combinatorial search space of $N_D \cdot N_L \cdot N_U = 300$ feature permutations was tested, from which the top five permutations were chosen and ran in weighted mode to produce a total of ten optimised LB models. Finally, another optimised city model was developed, constrained to include no more features than the optimised LB model with the highest total feature count. In total, this results in an array of twelve optimised models along with two baseline models.

2.10 Model Variance Estimation and Statistical Significance Testing

2.10.1 Model Variance Estimation

The feature optimization scheme results in a set of models whose performance is optimal. However, all models trained so far have been subjected to the same random seed for shuffling in the data preprocessing steps. Accuracies obtained hereby are denoted as ${}_sR^2$ (cf. eqs. 2 and 3), with the subscript s indicating identical shuffling. This means that (1) inter-model variability based on ${}_sR_{avg}^2$ scores is likely due to different features and processing (LB vs. CB); and (2) ${}_sR_{avg}^2$ scores may not represent scores the model would deliver upon shuffling with different random seeds. To address the latter issue, each model was fitted onto the data ϵ_1 times with different random seeds, resulting in accuracy

distributions $R^2\{\mathcal{N}_{i,\epsilon_1}\}$ where $\mathcal{N}_{i,\epsilon_1}$ denotes the distribution of the ϵ_1 runs associated with model i . In this study $\epsilon_1 = 200$ was chosen, as this value is above minimal required sample size for the performed statistical test (cf. sec. 2.7.2) (Kim and Park, 2019), but application to other cities may require other ϵ_1 . The expectation values of the distributions $\mu(R_{\text{avg}}^2\{\mathcal{N}_{i,\epsilon_1}\})$ are more robust measures of model accuracies than the ${}_sR_{\text{avg}}^2$ scores. Through obtaining variance and skewness estimates, the distributions furthermore help to quantify the variability that may be expected from the models.

2.10.2 Statistical Significance and Normality Testing

Additionally, the distributions $R_{\text{avg}}^2\{\mathcal{N}_{i,\epsilon_1}\}$ may be used to infer statements on the statistical significance of the results. For any pair of models M_i, M_j with accuracy distributions $R_{\text{avg}}^2\{\mathcal{N}_{i,\epsilon_1}\}, R_{\text{avg}}^2\{\mathcal{N}_{j,\epsilon_1}\}$, a paired t -test is performed in which the two distributions are tested against the null hypothesis of having identical means. The difference of means $\Delta\mu_{ij} \equiv \mu(R_{\text{avg}}^2\{\mathcal{N}_{i,\epsilon_1}\}) - \mu(R_{\text{avg}}^2\{\mathcal{N}_{j,\epsilon_1}\})$ is considered statistically significant if the p -value associated with the t -test is $p \leq 0.005$ (Benjamin et al., 2018). This procedure results in a probability of obtaining the observed or extremer differences in means between models M_i, M_j when the null hypothesis is true. Using p -values, any model M_i may be furthermore tested against the null hypothesis that its accuracy distribution is normal. Statistical significance again requires $p < 0.005$.

2.11 Model Application for Mitigation Potential Estimation

To assess the mitigation potential associated with the *n_U U-features over UAs — for LUT 13 (urban and built-up), that is — the testing data of each feature *f_k included in the optimal U-feature set for LUT 13 $F({}^*n_U) = \{ {}^*f_k \}_{k=1}^{*n}$ may be increased or decreased by a value ${}^\uparrow\Delta_k$ or ${}^\downarrow\Delta_k$, respectively. Both altering a single U-features or varying several U-features simultaneously is possible. The change in the target value $\Delta\hat{T}_i$ for model i and target T — either T2 or TSK — is then estimated as the difference between average predictions from non-varied and varied U-features. From this, a target sensitivity $\Delta\hat{T}_i \delta_{{}^*f_k}^{-1}$ towards unit change of *f_k , that is $\delta_{{}^*f_k}^{-1}$, may be estimated via

$$\Delta \hat{T}_i \delta_{*f_k}^{-1} = \frac{\partial \Delta \hat{T}_i}{\partial *f_k} \approx \frac{\Delta \hat{T}_i(*f_k + \uparrow \Delta_k) - \Delta \hat{T}_i(*f_k - \downarrow \Delta_k)}{\uparrow \Delta_k - \downarrow \Delta_k} \quad (4)$$

The average prediction for varied U-features is obtained through running an ensemble of model i comprising $\epsilon_2 = 200$ runs, resulting in model distributions $\mathcal{N}_{i, \epsilon_2=200}$. With $\epsilon_2 = \epsilon_1 = 200$, there are enough samples to permit statistical significance testing (Kim and Park, 2019), although these were not performed in this study. To account for different behaviour between day periods (06:00 – 21:59) and night periods (22:00 – 05:59) (Chen et al., 2014), these may be treated separately, but a total response across the full diurnal cycle may be computed as well. A detailed overview over the methodology is available in the supplementary materials (cf. sec. 7.3).

3 Results

The results of this study may be structured into four subsections. The first one will describe the results of the baseline models — based on ${}_sR_{\text{avg}}^2$ scores — and how these were used to find optimal feature sets. Thereafter, a statistical analysis — pertaining to $R_{\text{avg}}^2\{\mathcal{N}_{i, \epsilon_1}\}$ scores — is provided in which expected model variance and optimal model selection is presented. The subsequent subsection outlines how selected optimal models behave under different number of included HW data hours, while the final subsection consists of results of applying the selected optimal models to estimate mitigation potentials.

3.1 Baseline Models, Feature Selection and Feature Set Optimization

The baseline models result in ${}_sR_{\text{avg}}^2$ accuracies of 0.8163 and 0.8084 for $M_{C,0}$ and $M_{L,0}$, respectively. Employing these baseline models and using the methodology proposed in sec. 2.7, FIOs for the CB and LB models were found (FIOs are listed in supplementary materials tables 4 and 5, respectively) and used to find optimal feature sets using the approach outline in sec. 2.8. For CB models, a relationship of test ${}_sR_{\text{avg}}^2$ with changing numbers of included features n_t may be obtained (fig. 3abc). Fig. 3a shows that ${}_sR_{\text{avg}}^2$ is very low for $n_t = 1$ but increases rapidly. A local optimum is reached at $n_t = 7$ ($M_{C,B}^{(7)}$),

and after a slight performance dip a global maximum at $n_t = 19$ ($M_{C,B}^{(19)}$) is reached. This behaviour is similar for T2 (fig. 3b) and TSK (fig. 3c) and is in line with reported supervised feature selection behaviour (Cai et al., 2018). Likely, too few features contain insufficient

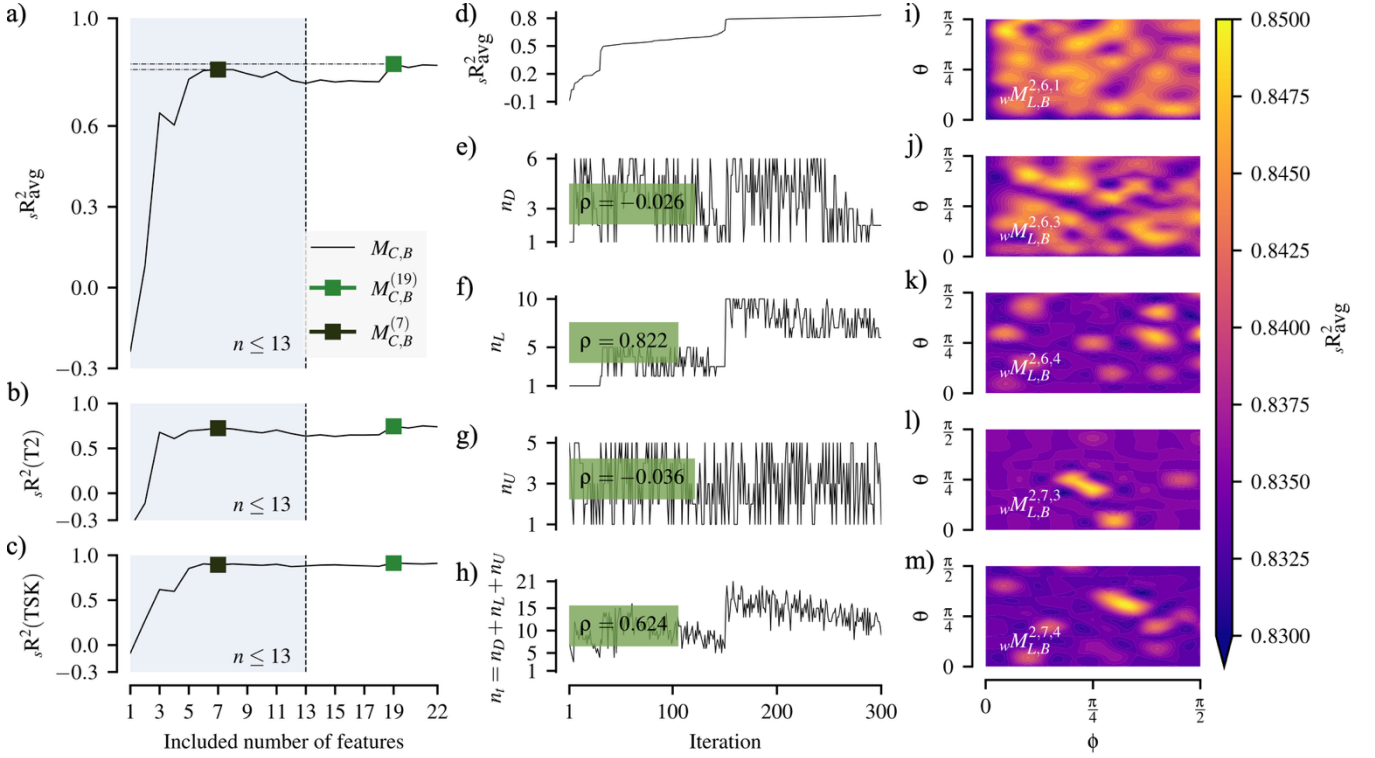


Figure 3: a – c: the change in accuracy when varying the number of included features from the FIO for the CB model. The baseline model $M_{C,0}$ herein refers to the very last model with 22 features included. d – h: the change in accuracy when varying the number of included driving-, local- and urban features for the LB non-weighted model, ordered here in ascending accuracy. Note that correlations between the number of included features and the accuracy is reported. Iteration here refers to a particular combination (n_D, n_L, n_U) . i – m: the variation of accuracy across ϕ, θ -space (cf. sec. 3.5) of the top 5 non-weighted models from panel B, i.e. representing the weighted models. The displayed values stem from a 11×11 grid which has been interpolated using cubic interpolation. Models decrease in accuracy from top down.

signal for RF-XGB to learn targets, while too many features may cause overfitting to unimportant features.

Fig. 3d shows the accuracy of $M_{L,0}$ when testing all 300 possible permutations of included driving-, local- and urban- features, displayed in order of ascending sR_{avg}^2 . Figures 3e-h show the pertaining

number of D-, L-, U-features as well as n_t . The ${}_sR_{\text{avg}}^2$ curve in fig. 3d has two discontinuities at about iterations 40 and 150 that seem to coincide with discontinuities in n_L (local features). As furthermore suggested by the highest correlations coefficients — displayed as ρ on figs. 3e-h and indicating the correlation coefficient between n_D , n_L , n_U or n_t and ${}_sR_{\text{avg}}^2$, respectively — of local features with ${}_sR_{\text{avg}}^2$, this is strong evidence that L-features may have high impact and are thus critical for building reliable urban climate ML models. As they represent influences across various scales and constitute the largest category, identifying L-features as highly important is intuitively coherent. Ideally, the proposed methodology should reflect such importance in category weights. To determine these, the top five permutations in figs. 3e-h, ${}_{nw}M_{L,B}^{2,6,1}$, ${}_{nw}M_{L,B}^{2,6,3}$, ${}_{nw}M_{L,B}^{2,6,4}$, ${}_{nw}M_{L,B}^{2,7,3}$ and ${}_{nw}M_{L,B}^{2,7,4}$, with respective ${}_sR_{\text{avg}}^2$ scores of 0.8414, 0.8321, 0.8319, 0.8302 and 0.8302 were selected to be run in weighted mode.

The ${}_sR_{\text{avg}}^2$ accuracies of the pertaining weighted models ${}_wM_{L,B}^{2,6,1}$, ${}_wM_{L,B}^{2,6,3}$, ${}_wM_{L,B}^{2,6,4}$, ${}_wM_{L,B}^{2,7,3}$ and ${}_wM_{L,B}^{2,7,4}$ in function of $\phi - \theta$ space are shown in figs. 3i-m and are 0.8462, 0.8393, 0.8332, 0.8328 and 0.8335, respectively. Within the ${}_sR_{\text{avg}}^2$ metric, weighted models outperform non-weighted models.

“Better” models like ${}_wM_{L,B}^{2,6,1}$, ${}_wM_{L,B}^{2,6,3}$ (figs. 3ij) are less sensitive to weighting than “worse” models like ${}_wM_{L,B}^{2,7,3}$, ${}_wM_{L,B}^{2,7,4}$ (fig. 3lm) that exhibit discernible ${}_sR_{\text{avg}}^2$ peaks towards $\phi = \theta = \pi/4$. Therefore,

“worse” models may perform well and almost equalate “better” models when an appropriate set of weights is found and adopted. Using eq. (4), the weights pertaining to these “worse” models are approximately $w_D = w_L = 0.5$ and $w_U = \sqrt{2}/2 = 0.71$, indicating highest weight of urban features.

With respect to the influence of L-features on non-weighted models discussed above (fig. 3f), local features seem to be of slightly lower importance. Meanwhile, U-features that are slightly anti-correlated with ${}_sR_{\text{avg}}^2$ in fig. 3g here exhibit relatively high importance. This may be evidence that the proposed weighting may adjust the influence of different categories on target estimates compared to non-weighted models.

These results suggest that optimised LB models outperform optimal CB models, and that weighted models outperform non-weighted models in the ${}_sR_{\text{avg}}^2$ metric. The proposed feature selection methodology therefore produces coherent results that may be used for feature set optimization. Such feature set optimization highlights the importance of local features and shows that weighting may act as an adjustment method to inform differential impacts of categories. Finally, weighting may have less impact for “better” models than for “worse” models. Underlying ${}_sR_{\text{avg}}^2$ scores are listed in table 1.

3.2 Model Variance, Statistical Significance and Optimal Models

Table 1: Overview over the main models. Listed models include baseline models $M_{C,0}$ and $M_{L,0}$ (indicated by subscript “0”), optimised CB model $M_{C,B}^{(19)}$, $M_{C,B}^{(7)}$ including 19 and 7 features (indicated by superscripts “19” and “7”), respectively; the optimal non-weighted- and weighted LB models ${}_{nw}M_{L,B}$, ${}_wM_{L,B}$ with various numbers of included features (indicated by subscripts “nw” and “w”). Columns: $n_T = n_D + n_L + n_U$; Weights w_D, w_L, w_U pertaining to D-, L- and U-features; ${}_sR_{\text{avg}}^2$ gives scores with same random shuffling seed; $\mu(R_{\text{avg}}^2\{\mathcal{N}_{\epsilon_1=200}\})$, $\sigma(R^2\{\mathcal{N}_{200}\})$ refer to mean and standard deviation of accuracies from model distribution $\mathcal{N}_{\epsilon_1=200}$; $P_N(R_{\text{avg}}^2\{\mathcal{N}_{\epsilon_1=200}\})$ refers to the p -value of testing the distribution against the null hypothesis of being normally distributed. $\mathcal{N}_{\epsilon_1=200}$ obtained by running models $\epsilon_1 = 200$ times with different random seeds for shuffling. Fields containing “-” indicate that the column value is not available for the pertaining model.

Model	n_D	n_L	n_U	n_T	w_D	w_L	w_U	${}_sR_{\text{avg}}^2$	$\mu(R_{\text{avg}}^2\{\mathcal{N}_{\epsilon_1=200}\})$	$\sigma(R_{\text{avg}}^2\{\mathcal{N}_{\epsilon_1=200}\})$	$P_N(R_{\text{avg}}^2\{\mathcal{N}_{\epsilon_1=200}\})$
$M_{C,0}$	-	-	-	22	-	-	-	0.8163	0.8226	0.006253	0.5086
$M_{L,0}$	6	10	5	21	1	1	1	0.8084	0.8011	0.003496	0.0852
$M_{C,B}^{(19)}$	-	-	-	19	-	-	-	0.8302	0.8334	0.005692	0.2699
$M_{C,B}^{(7)}$	-	-	-	7	-	-	-	0.8096	0.8036	0.009162	0.2065
${}_{nw}M_{L,B}^{(2,6,1)}$	2	6	1	9	1	1	1	0.8414	0.8367	0.003161	0.3400
${}_{nw}M_{L,B}^{(2,6,3)}$	2	6	3	11	1	1	1	0.8321	0.8324	0.003289	0.8394
${}_{nw}M_{L,B}^{(2,6,4)}$	2	6	4	12	1	1	1	0.8319	0.8265	0.003288	0.8602
${}_{nw}M_{L,B}^{(2,7,3)}$	2	7	3	12	1	1	1	0.8302	0.8264	0.003581	0.9975
${}_{nw}M_{L,B}^{(2,7,4)}$	2	7	4	13	1	1	1	0.8302	0.8268	0.003499	0.1833

$wM_{L,B}^{(2,6,1)}$	2	6	1	9	0.9755	0.1545	0.1564	0.8462	0.8359	0.003369	0.7567
$wM_{L,B}^{(2,6,3)}$	2	6	3	11	0.9045	0.2939	0.3090	0.8393	0.8320	0.003191	0.7066
$wM_{L,B}^{(2,6,4)}$	2	6	4	12	0.0000	0.8090	0.5878	0.8332	0.8268	0.003283	0.8589
$wM_{L,B}^{(2,7,3)}$	2	7	3	12	0.4156	0.4156	0.8090	0.8328	0.8259	0.003140	0.1300
$wM_{L,B}^{(2,7,4)}$	2	7	4	13	0.3673	0.7208	0.5878	0.8335	0.8256	0.003347	0.5748

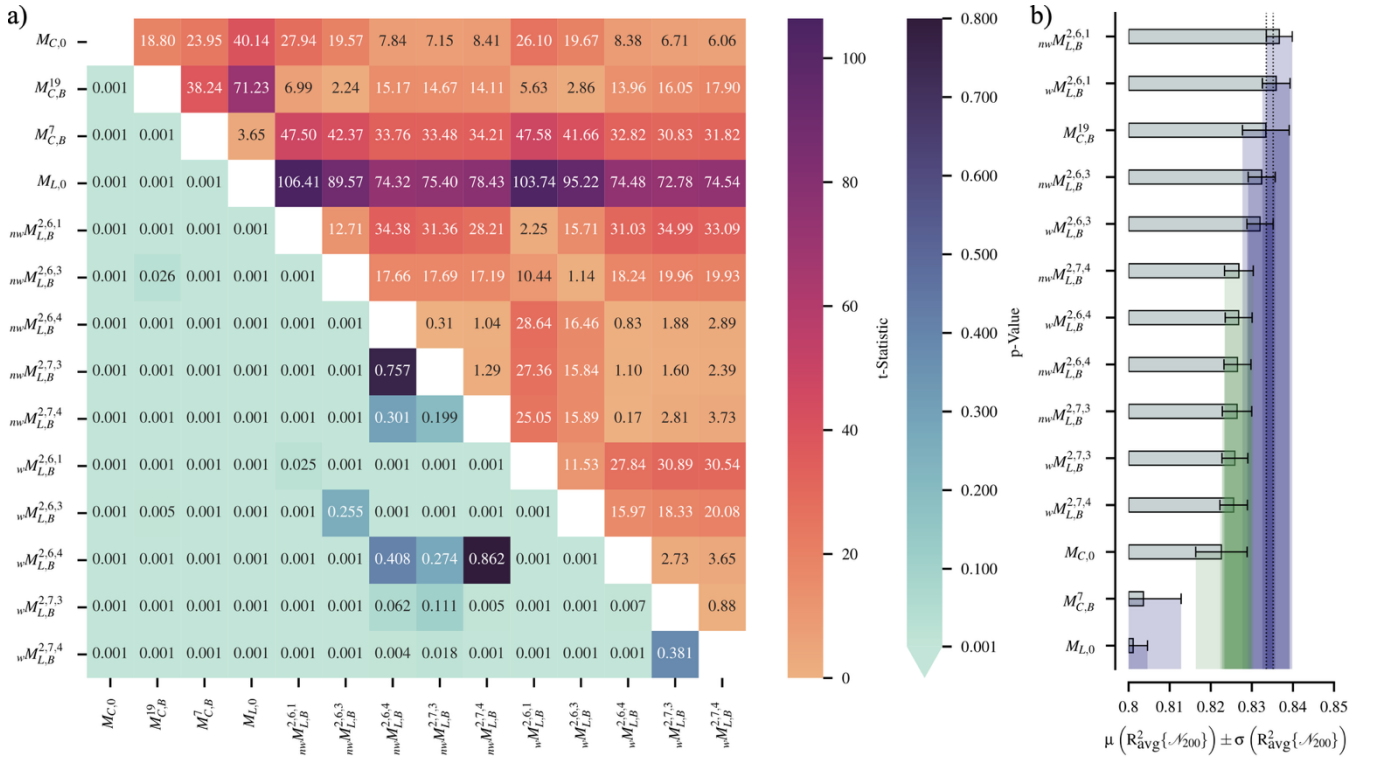


Figure 4: **a:** Upper triangular heatmap showing the t -statistics of pairwise testing the models against the null hypothesis of identical means, lower triangular heatmap showing the pertaining p -values. **b:** Accuracies of the models in descending order, with blue ribbons indicating standard deviations of the models, and the dashed area indicating the overlap of the $\mu(R_{\text{avg}}^2\{\mathcal{N}_{\epsilon_1=200}\}) \pm \sigma(R_{\text{avg}}^2\{\mathcal{N}_{\epsilon_1=200}\})$ area of the top 5 models. The green ribbons and the other blue ribbons from the worst-performing models exhibit an overlap that is spatially disjoint from the overlap of the top five models.

To inform on the expected intra-model variability, each model was ran $\epsilon_1 = 200$ times with different random data shuffling seeds to produce model distributions $\mathcal{N}_{\epsilon_1=200}$. Figure 4a shows the t -statistics and p -values of pairwise testing of means $\mu(R_{\text{avg}}^2\{\mathcal{N}_{\epsilon_1=200}\})$ of the underlying distributions against the null hypothesis of being identical. Pertaining p -values were displayed as 0.001 if they were smaller than

0.001 in fig. 4a. In addition to these p -values, table 1 also provides the p -values of testing the distributions against the null hypothesis of normal distribution, $p_N(\mathbb{R}_{\text{avg}}^2\{\mathcal{N}_{\epsilon_1=200}\})$, ranging between $0.0852 \leq p_N(\mathbb{R}_{\text{avg}}^2\{\mathcal{N}_{\epsilon_1=200}\}) \leq 0.9975$. Under the assumed significance threshold of 0.005, this statistic thus suggests that all distributions are likely to very likely normal or near-normal. Likewise, only few pairs of models have $\mathcal{N}_{\epsilon_1=200}$ -distributions whose means are not statistically significantly distinct. Noteworthy exceptions to this are ${}_{nw}M_{L,B}^{(2,7,4)}$ and ${}_wM_{L,B}^{(2,6,4)}$ ($p = 0.862$) as well as ${}_{nw}M_{L,B}^{(2,7,3)}$ and ${}_{nw}M_{L,B}^{(2,6,4)}$ ($p = 0.757$) which are the only two pairs with p -values above 0.5. There are an additional 10 combinations of models where $0.5 > p > 0.001$ (weak to moderate evidence to statistically significant differences in means) followed by the remaining 98 combinations where $p < 0.001$ (strong evidence of statistically significant differences in means). These results suggest that most model differences are statistically significant. Where such statistically significant effects are present, the observed effects are therefore likely due to inclusion of different features and not due to variability within the models.

The accuracies $\mu(\mathbb{R}_{\text{avg}}^2\{\mathcal{N}_{\epsilon_1=200}\}) \pm \sigma(\mathbb{R}_{\text{avg}}^2\{\mathcal{N}_{\epsilon_1=200}\})$, are visualised in figure 4b. The absolute difference between distribution mean accuracy and ${}_s\mathbb{R}_{\text{avg}}^2$ score, $\Delta R^2 = |\mu(\mathbb{R}_{\text{avg}}^2\{\mathcal{N}_{\epsilon_1=200}\}) - {}_s\mathbb{R}_{\text{avg}}^2|$ is larger than the standard deviation, i.e. $\Delta R^2 > \sigma(\mathbb{R}_{\text{avg}}^2\{\mathcal{N}_{\epsilon_1=200}\})$, for all models but $M_{C,B}^{(19)}$, $M_{C,B}^{(7)}$, ${}_{nw}M_{L,B}^{(2,6,3)}$ and ${}_{nw}M_{L,B}^{(2,7,4)}$. The largest difference pertains to ${}_wM_{L,B}^{(2,6,1)}$ and is $\Delta R^2 = 3.049\sigma(\mathbb{R}_{\text{avg}}^2\{\mathcal{N}_{\epsilon_1=200}\})$, with mean and median deviations across all models of $\Delta R^2 = 1.5308\sigma$ and $\Delta R^2 = 1.5702\sigma$, respectively. Assuming normally distributed $\mathbb{R}_{\text{avg}}^2\{\mathcal{N}_{\epsilon_1=200}\}$ — justified by $p_N(\mathbb{R}_{\text{avg}}^2\{\mathcal{N}_{\epsilon_1=200}\})$ values — it can be expected that 68% of ${}_s\mathbb{R}_{\text{avg}}^2$ scores lie within $(\mathbb{R}_{\text{avg}}^2\{\mathcal{N}_{\epsilon_1=200}\}) \pm \sigma(\mathbb{R}_{\text{avg}}^2\{\mathcal{N}_{\epsilon_1=200}\})$. The observed value is only 28.6%, implying that ${}_s\mathbb{R}_{\text{avg}}^2$ scores are generally not contained in the $\mu \pm \sigma$ range of the associated distributions.

Although ΔR^2 may not behave as expected, within the five most accurate models ${}_{nw}M_{L,B}^{(2,6,1)}$, ${}_{w}M_{L,B}^{(2,6,1)}$, $M_{C,B}^{(19)}$, ${}_{nw}M_{L,B}^{(2,6,3)}$ and ${}_{w}M_{L,B}^{(2,6,3)}$ in order of descending accuracy, the two top-performing LB models ${}_{nw}M_{L,B}^{(2,6,1)}$ and ${}_{w}M_{L,B}^{(2,6,1)}$ outperform the top performing CB model $M_{C,B}^{(19)}$. The differences in $\mu(R_{\text{avg}}^2\{\mathcal{N}_{\epsilon_1=200}\})$ between these models are statistically significant ($p \leq 0.005$). After these five “top” models follow seven models of similar albeit lower accuracy. After these “intermediate” models follow two “worst” models — $M_{C,B}^{(7)}$ and $M_{L,0}$. “Top”-, “intermediate”- and “worst” models are distinct: any model contained in any accuracy group predicts statistically significantly different means $\mu(R_{\text{avg}}^2\{\mathcal{N}_{\epsilon_1=200}\})$ than any model from any other group.

To assess mitigation potentials, high-performing ML models with high number of urban — or modifiable — features are desirable. When considering the “top” group, models including three U-features underperform models with a single U-feature. This gives rise to a trade-off: shall the model with highest accuracy or with highest number of U-features be picked?

As can be seen from fig. 4b, $\mu(R_{\text{avg}}^2\{\mathcal{N}_{\epsilon_1=200}\}) \pm \sigma(R_{\text{avg}}^2\{\mathcal{N}_{\epsilon_1=200}\})$ of the “top” models overlap between $0.8335 \leq \mu(R_{\text{avg}}^2\{\mathcal{N}_{\epsilon_1=200}\}) \leq 0.8352$. Assuming normal distributions of the “top” models — justified by $p_N(R_{\text{avg}}^2\{\mathcal{N}_{\epsilon_1=200}\})$ in table 1 — the probability of any top-five model to produce a score within the overlap, $P_i(O)$, ranges between 11.5% and 17.6% (cf. fig. 7 supplementary material). Once in the overlap, the probability that the score can be attributed to the i -th model is

$$P(O \wedge M_i) = \frac{P_i(O)}{\sum_i P_i(O)} \quad (5)$$

$P(O \wedge M_i)$ is maximal for to ${}_wM_{L,B}^{(2,6,1)}$ at 22.6% and minimal for $M_{C,B}^{19}$ at 14.8%. This means that a score in the overlap may in 77.4% of cases have been produced by the “best” of the “top” models (${}_{nw}M_{L,B}^{(2,6,1)}$ and ${}_wM_{L,B}^{(2,6,1)}$) or the “worst” of the “top” models (${}_{nw}M_{L,B}^{(2,6,3)}$ or ${}_wM_{L,B}^{2,6,3}$). The maximal expected accuracy loss between “best” and “worst” of the “top” models (cf. table 1) is $\Delta\mu(R_{\text{avg}}^2\{\mathcal{N}_{\epsilon_1=200}\}) = 0.0047 \pm 0.0064$ (likely statistically significant as “top” and “worst” of the “top” models are statistically significantly different at $p = 0.001$) when assuming σ to be an appropriate estimation of the model uncertainty — which is perhaps not certain given the unexpected behaviour of ΔR^2 . This loss is only slightly bigger than $\sigma(R_{\text{avg}}^2\{\mathcal{N}_{\epsilon_1=200}\})$ of “top” and “worst” of the “top” models — and may therefore have been produced through the internal variability of the model. This suggests that the nominally “worst” of the “top” models with three urban features may be used instead of the “top” of the “top” models with only one urban feature, because associated accuracy losses (1) occur only *sometimes*; and (2) are likely small. Urban planners thereby gain two urban features — $M_{L,B}^{(2,6,1)}$ contain emissivity as the sole U-feature whereas $M_{L,B}^{(2,6,3)}$ contains the three U-features emissivity (EMISS), albedo (ALBEDO) and leaf area index (LAI) — that they may use to mitigate UHIs.

Within these “top” of the “worst” of the “top” models — ${}_{nw}M_{L,B}^{(2,6,3)}$ and ${}_wM_{L,B}^{2,6,3}$ — shall the weighted or the non-weighted model be chosen to assess mitigation potentials? Although the results from weighting in the ${}_sR_{\text{avg}}^2$ metric and suggest that weighting improves performance, employing the $R_{\text{avg}}^2\{\mathcal{N}_{\epsilon_1=200}\}$ metric yields that weighting is likely statistically insignificant: observed differences in $\mu(R_{\text{avg}}^2\{\mathcal{N}_{\epsilon_1=200}\})$ between weighted- and non-weighted LB models are associated with high p -values of 0.255 for “worst” (${}_{nw}M_{L,B}^{(2,6,3)}$ and ${}_{nw}M_{L,B}^{(2,6,3)}$) (very likely statistically insignificant), and 0.025 for “top” (${}_{nw}M_{L,B}^{(2,6,1)}$ and ${}_{nw}M_{L,B}^{(2,6,1)}$) (likely statistically insignificant) of the “top” models. Likewise, within “intermediate” models, only one out of three configuration ($M_{L,B}^{(2,7,4)}$) shows statistically significant

differences between weighted and non-weighted models. Therefore, even though weighted models outperform non-weighted models in the sR_{avg}^2 metric, the weighted “worst” model shall here be disregarded in favour of the non-weighted “worst” model to assess mitigation potentials.

3.3 Impact of Number of Heat Wave Hours in Training Data

Having selected an optimal model — the non-weighted “worst” of the top models $_{nw}M_{L,B}^{(2,6,3)}$ — what is the optimal number of included heatwave data hours in the training set, and is this optimal number robust across other models? For the five “top” models, figures 5a-c and 5d-f show the evolution of sR^2 accuracies for including various portions of 2017 heatwave data hours in the training set, always evaluated against the 2019 heatwave testing data, for the entire domain (fig. 5a-c) and for LUT 13 (urban- and built-up) only (fig. 5d-f), respectively. There are two general trends: first, there is a clear upwards trend of accuracy for both the entire domain and LUT 13 with increasing number of included heatwave hours. This trend is first rather small but increases towards the maximal number of included heatwave data. Secondly, for both the entire domain and LUT 13, the predictions in T2 contain more variability than the predictions for TSK (note the different axis scaling). The highest accuracies are universally observed when using the maximal hours of heatwave data. These results suggest that including more heatwave data increases the accuracy, both for T2 and TSK, and for “top” models. Importantly, all predictions have been obtained using HPs tuned on the maximal number of 2017 HW data hours, and the largest increase in accuracy universally occurs from 144h to 168h in figs. 5a-f. Because the distributions of feature data between 144h and 168h of included HW data are supposedly similar, HP tuning *should* give similar HPs when tuned on 144h or 168h. As it is within this range, however, that the largest increases in accuracy occur when HPs are kept the same, it is more probable that increases stem from inclusion of more HW data rather than from HP tuning effects.

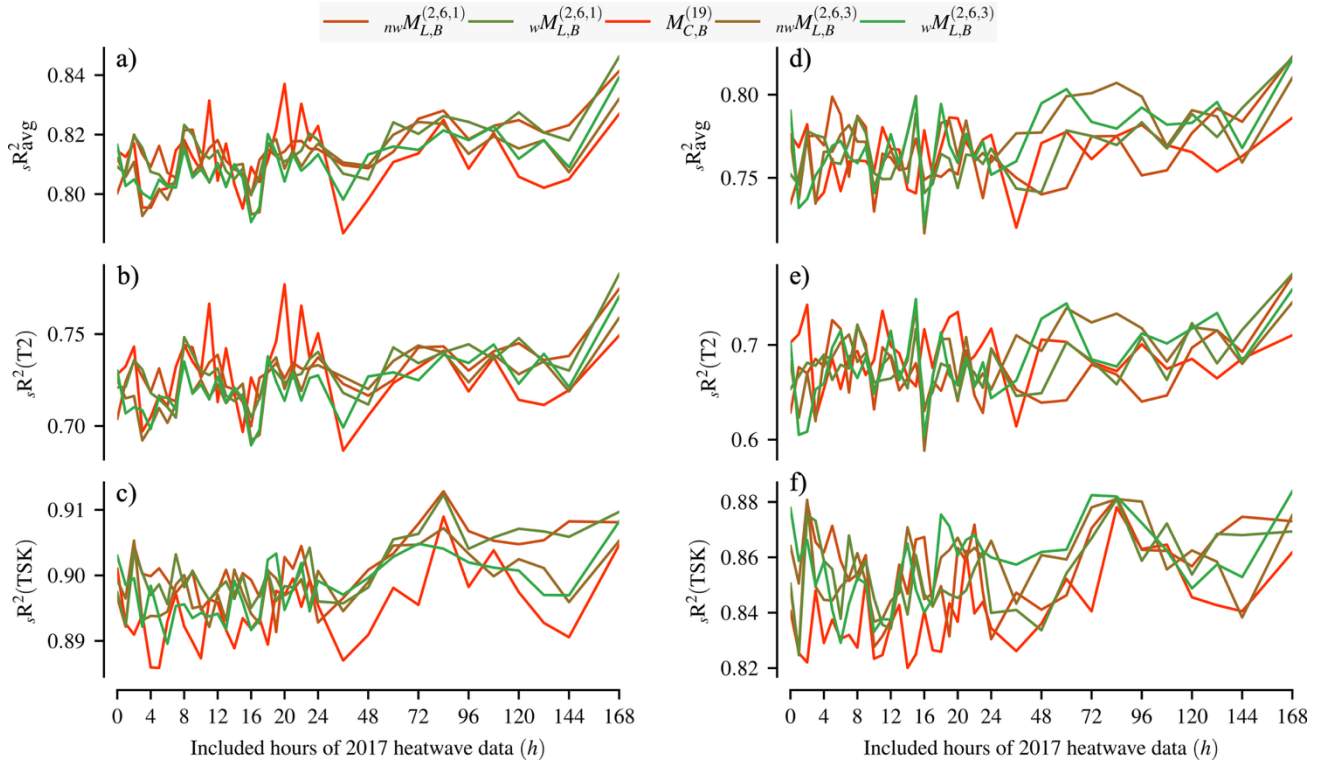


Figure 5: a-c: Including various hours of 2017 heatwave data in the training process, showing the combined- (a), T2- (b) and TSK-(c) accuracy, for the entire working domain. d-f: The same as in panel A, but only for LUT 13, urban and built-up.

3.4 Model Application to Estimate Mitigation Potentials

The non-weighted “worst” of the “top” models $nwM_{L,B}^{(2,6,3)}$ was used to estimate the sensitivities of T2 and TSK towards variations in the included U-features emissivity, albedo and LAI, following the methodology in sec. 2.11. These pertain to the top three U-features from the FIO (table 5). The imposed variations were chosen such that “realistic” values resulted: for EMISS $\{\uparrow\Delta_{\text{EMISS}}, \downarrow\Delta_{\text{EMISS}}\} = \{-0.38, 0.013\}$ such that varied EMISS is within $[0.5, 0.998]$, for ALBEDO $\{\uparrow\Delta_{\text{ALBEDO}}, \downarrow\Delta_{\text{ALBEDO}}\} = \{-0.02, 0.25\}$ such that varied ALBEDO is within $[0.1, 0.982]$, and for LAI $\{\uparrow\Delta_{\text{LAI}}, \downarrow\Delta_{\text{LAI}}\} = \{-0.5, 5\}$ such that varied EMISS is within $[0.5, 6]$. The results are displayed in fig. 6 for T2 and fig. 7 for TSK. Pertaining gradients are listed in table 2.

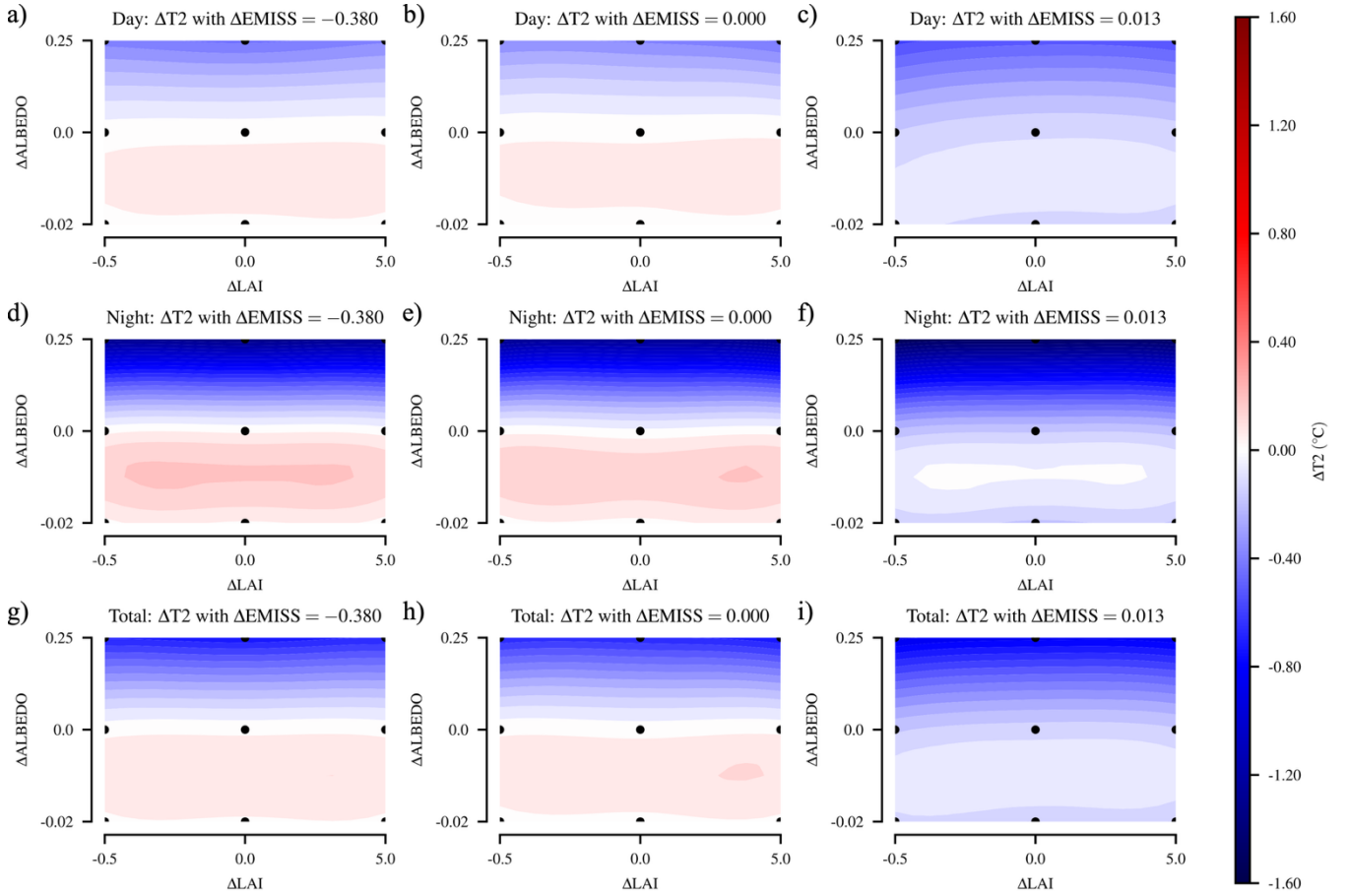


Figure 6: a-i: Heatmaps for T2 resulting from applying the model $_{nw}M_{L,B}^{(2,6,3)}$ with a variable shift in the value of the top three urban features. Black dots indicate the points in the feature space where the model was evaluated, with the heatmap having been interpolated using cubic interpolation between the grid points. **a-c:** Response to variations during daytime (06:00 – 21:59). **d-f:** Response to variations during the nighttime (22:00 – 05:59). **g-h:** Total response to variations over the entire day.

For all EMISS values tested, and for the daytime-, nighttime- and total response, there is a strong dependency of the T2-response on ALBEDO variation, while the dependency on LAI appears weak (fig. 6). Similar behaviour is visible for TSK (fig. 7), although variation with ALBEDO appears weaker and variations with LAI seem more pronounced. Furthermore, variations of T2 with ALBEDO appear lower during the day than during night, and EMISS variation response seem to have opposite effect for T2 and TSK.

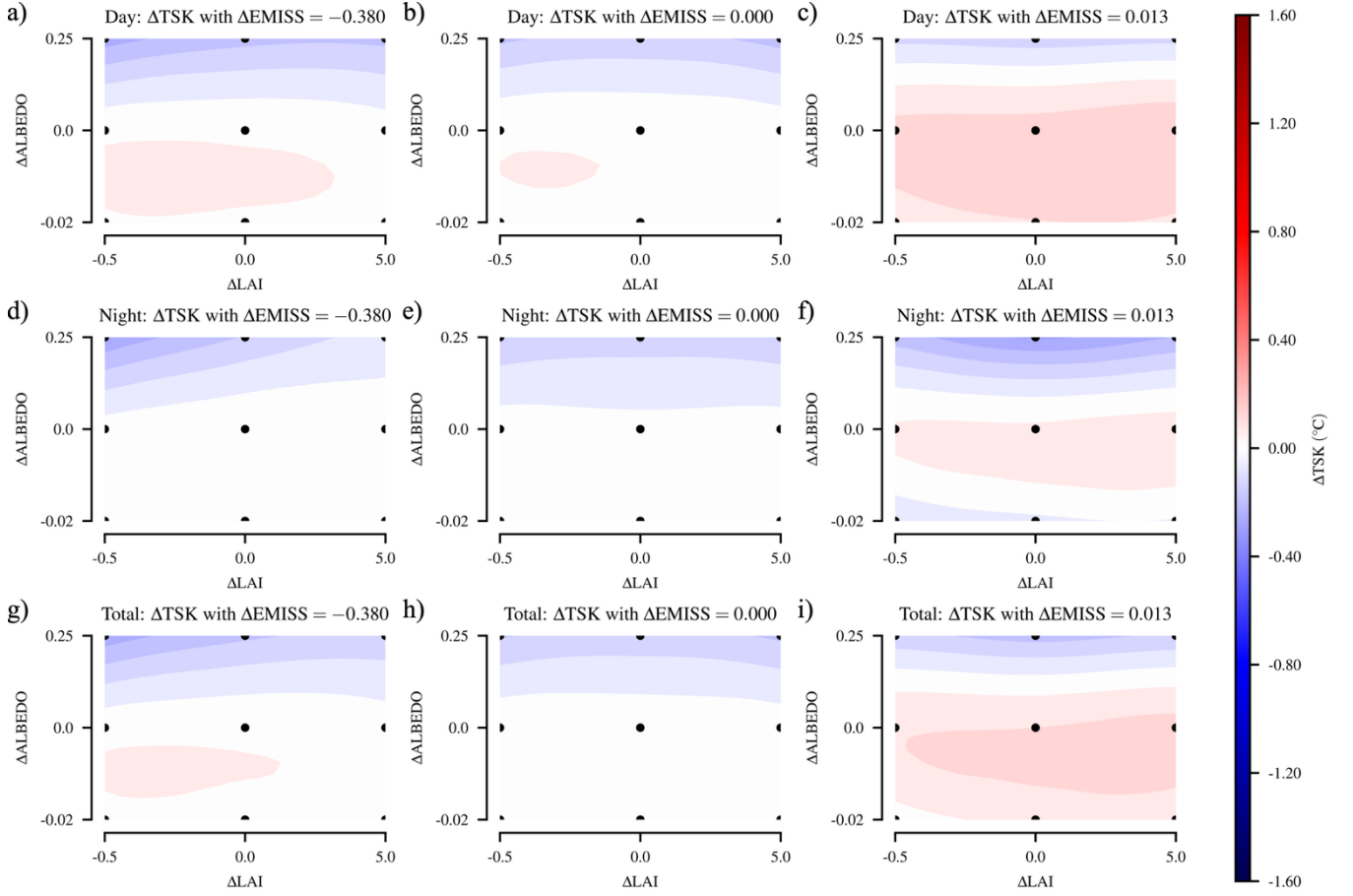


Figure 7: as in fig. 6, but for TSK. **a-i:** Heatmaps for TSK resulting from applying the model $_{nw}M_{L,B}^{(2,6,3)}$ with a variable shift in the value of the top three urban features. Black dots indicate the points in the feature space where the model was evaluated, with the heatmap having been interpolated using cubic interpolation between the grid points. **a-c:** Response to variations during daytime (06:00 – 21:59). **d-f:** Response to variations during the nighttime (22:00 – 05:59). **g-h:** Total response to variations over the entire day.

Table 2: Overview over model application results, showing variation in target prediction $\Delta\hat{T}$ per unit feature change δ_f .

Period	$\Delta\hat{T} \delta_{EMISS}^{-1}$ (°C)	$\Delta\hat{T} \delta_{ALBEDO}^{-1}$ (°C)	$\Delta\hat{T} \delta_{LAI}^{-1}$ (°C)
<i>T2</i>			
Day	-0.3018 ± 0.0184	-1.4105 ± 0.0277	0.0010 ± 0.0013
Night	-0.4904 ± 0.0202	-4.7893 ± 0.0363	-0.0005 ± 0.0014
Total	-0.3647 ± 0.0183	-2.5368 ± 0.0284	0.0005 ± 0.0013
<i>TSK</i>			
Day	0.2727 ± 0.0316	-0.5527 ± 0.0466	-0.0028 ± 0.0023
Night	0.0779 ± 0.0203	-0.4146 ± 0.0280	-0.0006 ± 0.0013
Total	0.2078 ± 0.0310	-0.5067 ± 0.0453	-0.0020 ± 0.0022

Measured sensitivities (cf. table 2) indicate similar results: the strongest cooling impact — or negative sensitivity — is observed for ALBEDO both for T2 and TSK, while EMISS responses differ in sign between T2 and TSK but are of largely similar magnitude. Effects of LAI are so low that uncertainties mostly do not permit determining the sign of the response, implying that response to LAI may be too low to be captured against the natural variability of the model used.

The magnitude of ALBEDO and EMISS response is up to 1 order of magnitude lower than computed in previous studies (Giannaros et al., 2018). Furthermore, as outlined in (Giannaros et al., 2018), higher emissivity should lead to lower T2 and lower TSK through higher radiative cooling, but while a strong cooling effect is observed for T2, TSK seems to increase. Together, these results suggest that mitigation strategies may lead to slightly different behaviour during the night, and that T2 and TSK may respond differently to the same mitigation strategy.

4 Discussion

The first aim of this study is to show that HW data is required to predict HW events, and that NHW data alone may be insufficient. This has been shown in fig. 6ab, both globally and for urban- and built-up areas, with more HW data increases accuracy. The second aim of this study is to demonstrate that LB models outperform CB models. The results obtained indicate that at least one optimised LB model outperforms its CB counterpart in both ${}_sR_{\text{avg}}^2$ and $\mu(R_{\text{avg}}^2\{\mathcal{N}_{\epsilon_1=200}\})$ metrics, with ${}_sR_{\text{avg}}^2$ scores usually higher than the more robust $\mu(R_{\text{avg}}^2\{\mathcal{N}_{\epsilon_1=200}\})$ scores but usually not contained within $\mu(R_{\text{avg}}^2\{\mathcal{N}_{\epsilon_1=200}\}) \pm \sigma(R_{\text{avg}}^2\{\mathcal{N}_{\epsilon_1=200}\})$. The third aim of this study is to demonstrate that LB models employing feature categorization and feature inclusion using FIOs lead to better results and higher interpretability. The results show that LB models employing this framework may outperform CB and LB models that do not employ the framework, emphasising that FIOs may contribute meaningful feature

ranking schemes across scales. Finally, based on statistical arguments, an optimal model was selected to demonstrate how mitigation potentials of urban features may be estimated.

For this application, a non-weighted rather than a weighted model was selected, because weighting is likely statistically insignificant, or more precisely: within the $\mu(R_{\text{avg}}^2\{\mathcal{N}_{\epsilon_1=200}\})$ metric, differences between weighted and non-weighted models were statistically insignificant. This means that within the $\mu(R_{\text{avg}}^2\{\mathcal{N}_{\epsilon_1=200}\})$ metric, there is no need to adapt special weights for categories to obtain optimal performance and capture the nature of the system. Weights $w_D = w_L = w_U = 1$ as implied by non-weighted models are sufficient, because RF-XGB in non-weighted mode appears robust in the $\mu(R_{\text{avg}}^2\{\mathcal{N}_{\epsilon_1=200}\})$ metric. The authors therefore recommend adapting $w_D = w_L = w_U = 1$.

As category weighting is a linear operation altering features values, feature space partition edges determining RF-XGB predictions may be subjected to the same transformation, effectively rendering RF-XGB weighting-invariant. An effect of weighting is still observed in the ${}_sR_{\text{avg}}^2$ metric, implying that such an invariance is likely only approximate. By averaging over large ensembles, such slight changes in performance may be “averaged away” or become small against internal variability through different random shuffling seeds. Other machine learning methods could potentially increase the significance of weighting in the $\mu(R_{\text{avg}}^2\{\mathcal{N}_{\epsilon_1=200}\})$ metric through resolving category weights explicitly instead of — indicated by the recommendation to use $w_D = w_L = w_U = 1$ — implicitly, although potentially at higher computational costs. This favours employing ensembles in the $\mu(R_{\text{avg}}^2\{\mathcal{N}_{\epsilon_1=200}\})$ metric to apply RF-XGB as an emulator. However, performance may be improved through other methodological adjustments concerning random shuffling and subsequent 10-fold CV: current preprocessing inhibits RF-XGB to learn any relevant physical process on time scales exceeding data temporal resolution and allows no lateral information flow between grid points. However, synoptic-scale processes are associated with longer time scales, and small-scale processes such as heating or runoff may have large

lateral flows. This may be especially important because local features, shaped by the properties of both large- and small scales, may be highly influential. Due to these interactions, assessment of spatial scale weights may be challenging when not including temporal evolution and lateral flow. The former may be achieved through embedding past timesteps as features (Gudmundsson and Seneviratne, 2015), the latter through convolutional neuronal networks that additionally learn directly on feature values.

All the same, the results obtained from applying the selected non-weighted model demonstrate mitigating effects of increased albedo, as proposed in literature (Giannaros et al., 2018). Albedo changes are easy-to-implement mitigation strategies and emphasise the high interpretability of the proposed methodology in terms of mitigation strategy design. Unexpected increases of TSK when increasing EMISS and indeterminate sensitivity of TSK to LAI could however limit the confidence in mitigation potential assessments through the proposed framework. If the underlying WRF-SLUCM model was forced at the land-atmosphere interface with remotely sensed radiological data for EMISS and TSK, this may lead to a tight functional relationship between EMISS and TSK. In that case imposing higher EMISS values may be misinterpreted by RF-XGB as *higher* TSK at unchanged *effective* emissivity. This may indicate that the model partially overfits, and that increasing EMISS may still have a meaningful mitigating effect. Although TSK is likely less important than T2 for human thermal discomfort (Heaviside et al., 2017), and T2 shows the expected sign of sensitivity towards EMISS, for the sake of accuracy, this unexpected TSK sensitivity to EMISS is important to address. Tighter constraints on response sensitivities through methodological improvements may not only inform on the observed unexpected sign of TSK response to EMISS variation, but also improve magnitude estimates towards previously reported values, especially for LAI.

Overall, despite limitations, the proposed method gives clear results indicating feature importances and associated mitigation potentials. This makes the results straightforward to interpret for urban planners.

To render the findings more robust, the method needs to be applied to more cities, because the results obtained in this study, and particularly the FIOs, are only applicable for the study WD of Zurich, and only for the present WRF-SLUCM output as training- and testing data. Other cities and other data configurations will very likely produce different results and different FIOs, and will require different preclassifications. This is equally true when including more features, different data sources, or resolving urban 3D spaces explicitly.

5 Conclusion

In this study, a ML emulator of WRF-SLUCM output was used to predict T2 and TSK for the city of Zurich, Switzerland. It proposes a novel method to assess the influence of features on different scales on UHIs and provides urban planners with a method to determine and quantify mitigation strategies for UHIs. This is achieved through preclassifying features into groups pertaining to a certain scale and degree of modifiability, employing a feature selection scheme based on SBS to create FIOs, and use feature set optimization to find model optimal configurations. Subsequently, the mitigation potential of the most modifiable and important features is determined. This study demonstrates (1) that RF-XGB to predict HWs in UAs performs better if more HW data is included in the training set; (2) that LB models distinguishing LUTs may outperform CB models not distinguishing LUTs; and (3) that LB models employing feature categorization and feature selection using LUT-specific FIOs may maximise performance and interpretability.

The results of this study are evidence that the proposed methodology may be applicable to characterise UHIs, and to assess the potential of mitigation strategies. The most important urban features identified in this study are emissivity, albedo and LAI. Signs of estimated sensitivities of T2 towards these are in line previous studies, even though different response magnitudes are observed. Sensitivities of TSK towards emissivity, and to a lesser degree LAI, may contradict previous studies and require further investigation. The results also indicate that weighting is likely not statistically significant, which may be partially due

to statistical discrepancies between ${}_sR_{\text{avg}}^2$ and $R_{\text{avg}}^2\{\mathcal{N}_{\epsilon_1=200}\}$ metric. Along with required evidence of robustness across different cities, the method needs to be improved with respect to overfitting and other methodological improvements in subsequent studies. The results of this study should be understood as evidence that the proposed method may yield meaningful, highly interpretable results for the city it is applied to.

It should be emphasised that the methodology is intended to be applicable for any UA, although it has been demonstrated only for Zurich. While it is therefore premature to make such general assertions, the results obtained for Zurich are evidence of the methods' general applicability. Future work should focus on testing the method on other cities to assess its efficiency and robustness on a larger set of UAs. Moreover, future work should focus on improving the methodology by using time-step embedding and convolutional neuronal networks, or other methods to include lateral flow and reenforce weighting impact, and address overfitting to reduce the respective insignificances and uncertainties associated with weighting and mitigation potential estimates.

6 Acknowledgements

The authors would like to thank Dominik Strebel for preparing the WRF-SLUCM model and making its output available.

7 Supplementary Material

7.1 Overview Over Features And Targets

Table 3: Features and Targets obtained from the WRF-SLUCM output for 2017, 2019 and combined 2017 + 2019. The presented data does not include LUT 17 (water). Shown are mean μ , standard deviation σ and skewness sk for the feature set for 2017 data, 2019 data and the combined 2017 + 2019 dataset.

Footnotes: ^a: driving features. ^b: local features. ^c: urban features.

Name	Description	Unit	2017			2019			2019 + 2017		
			μ	σ	sk	μ	σ	sk	μ	σ	sk
<i>Features</i>											
ALBEDO ^c	Surface Albedo	-	0.1675	0.0236	0.0990	0.1768	0.0515	4.6555	0.2769	0.1184	1.3864
CANWAT ^b	Foliage Canopy Water Content	kgm^{-2}	0.0161	0.0716	5.1394	0.1080	0.1785	1.4126	0.1412	0.1689	0.9974
COSZEN ^a	Zenith angle	rad	0.2895	0.4407	0.0084	0.2881	0.4403	2.2058e-5	0.2669	0.4347	0.0757
EMISS ^c	Emissivity	-	0.9469	0.0349	-1.0805	0.9470	0.0346	-1.0945	0.9542	0.0220	-1.7413
HGT ^a	Terrain Height	m	520.8086	88.7170	0.6643	520.8084	88.7170	0.6443	520.8086	88.7170	0.6643
ISLTYP ^a	Soil Type	-					<i>Categorical</i>				
IVGTYP ^c	Vegetation Type	-					<i>Categorical</i>				
LAI ^c	Leaf Area Index	m^2m^{-2}	4.1214	1.8139	-0.6957	4.1307	1.8066	-0.7254	4.7378	1.1546	-0.8191
LU_INDEX ^d	Land Use Type	-					<i>Categorical</i>				
LWDNB ^b	Longwave Radiation at Bottom	Wm^{-2}	365.0426	26.8786	-0.1434	349.0592	29.9627	-0.1395	351.3814	30.6930	-0.1449
PBLH ^b	Planetary Boundary Layer Height	m	351.4272	410.1020	1.2524	333.9043	372.0216	1.3355	470.1146	376.6531	1.0780
PSFC ^b	Surface Pressure	Pa	95977.5100	989.8087	-0.5968	95750.8800	1068.3694	-0.5169	95612.9000	1219.2892	-0.2974
QRAIN ^a	Rain Mixing Ratio	$kgkg^{-1}$	6.127E-7	2.0485E-5	61.1704	6.3888e-4	6.2328e-5	23.9743	4.4418e-5	1.5931e-4	9.2420
SFROFF ^b	Surface Runoff	mm	1.5562	2.0549	1.6003	13.8998	13.5140	1.3147	8.4936	11.6579	2.0135
SWDNB ^b	Shortwave Radiation at Bottom	Wm^{-2}	351.0178	366.3360	0.4579	325.3036	355.6135	0.5846	488.9915	332.0749	-0.0433
TMN ^b	Soil Temperature at Bottom	$^{\circ}C$	281.9639	0.5637	-0.5788	218.964	0.5637	-0.5791	281.9627	0.5666	-0.5772
U10 ^b	Wind Speed (10m above ground, u-direction)	ms^{-1}	0.3573	2.6807	-0.5871	-0.2331	2.5251	0.1457	-0.1389	2.5593	0.0239
UDROFF ^b	Underground Runoff	mm	30.2999	8.0227	-0.4292	147.6104	42.4052	-0.8758	127.6706	58.7390	-0.5682
V10 ^b	Wind Speed (10m above ground, v-direction)	ms^{-1}	-0.6268	2.0953	-0.1590	-0.9402	2.0878	0.3270	-0.8847	2.0932	0.2457
VAR ^a	Orographic Variance	-	106.6717	37.5529	2.0111	106.6717	37.5529	2.0111	115.7756	48.4775	1.2886
VAR_SSO ^a	Sub-Grid Orographic Variance	-	10669.8650	5269.0640	1.7840	10669.8640	5269.0635	1.7840	10669.8640	5269.0635	1.7840
VEGFRA ^c	Vegetation Fraction	-	73.1027	14.1765	-2.2747	73.0550	14.0191	-2.3906	73.5866	13.0102	-2.1425
<i>Targets</i>											
T2	Air Temperature (2m above ground)	$^{\circ}C$	23.8338	4.4820	-0.3103	20.2205	5.7111	0.0136	20.8521	6.4341	-0.1437
TSK	Surface Temperature	$^{\circ}C$	24.3853	6.7107	0.1850	20.8254	7.5817	0.1886	21.6946	8.2821	0.0707

7.2 Justification of Feature Categories

Driving features are solar zenith angle (COSZEN), terrain height (HGT), soil type (ISLTYP), rain mixing ratio (QRAIN), orographic variance (VAR) and subgrid orographic variance (VAR_SSO).

Clearly, solar zenith angle and terrain height are not modifiable by urban planners, as is the underlying soil type, even though UAs may partially or fully remove topsoil or render it impermeable through urban morphology. More difficult to assess is perhaps rain mixing ratio: this depends on temperature (rain evaporation), humidity, cloud cover and pressure. It is unlikely that any mitigation strategy might thus specifically target rain mixing ratio without feeding back onto these other parameters. Easier are (sub-grid-) orographic variance, because topography and orography are not in human control.

Local features include foliage canopy water content (CANWAT), longwave radiation at bottom (LWDNB), planetary boundary layer height (PBLH), surface pressure (PSFC), surface runoff (SFROFF), shortwave radiation at bottom (SWDNB), soil temperature at bottom (TMN), zonal wind 10 m above ground (U10), underground runoff (UDROFF) and meridional wind 10 m above ground (V10).

Canopy water content (CANWAT) may partially be controlled through the type of vegetation introduced, but background climate and geographic location, i.e. being in an arid or a humid climate, will greatly influence what kind of vegetation may be sustained. Longwave (LWDNB) and short wave radiation (SWDNB) is subject to the canopy content, itself subject to this geographic constraint.

Although canopy design may alter incoming and outgoing long- and shortwave radiation, geographic location will still be dominating in the radiation balance. The planetary boundary layer height (PBLH) is determined by atmospheric stability and the vertical potential temperature gradient. These are influenced by synoptic-scale weather, but also through urban-scale humidity and temperature modifications.

Similarly, the pressure (PSFC) is coupled to wind- (U10, V10) and temperature fields, again being somewhere in between large-scale and small-scale processes. Through construction and soil type, soil temperature (TMN) is largely controlled, but background climate will greatly matter here. Similarly, runoff (SFROFF, UDROFF) is determined partially by soil permeability, but also by precipitation and evapotranspiration which are large-scale processes eluding human control.

Urban features include albedo (ALBEDO), emissivity (EMISS), vegetation type (IVGTYP), leaf area index (LAI), and vegetation fraction (VEGFRA). Albedo (ALBEDO) and emissivity (EMISS) may be relatively easily controlled by choosing appropriate surface materials. Vegetation type (IVGTYP) and vegetation amount (VEGFRA, LAI) may be determined by urban planners upon plantation.

7.3 Detailed Methodology for Weighting of Categories

As weighting occurs after scaling, all weights $w_{D,L,U}$ are constrained to $w_{D,L,U} \in [0, 1]$ and to $w_{D,L,U} \geq 0$.

Assuming the respective ratios of the weights, rather than their absolute values, to be relevant, the weight vector may be further constrained to $\|\mathbf{w}\| = 1$. With this, the weight space may be parametrized using ϕ, θ -space:

$$w_D = \sin \theta \cos \phi, w_L = \sin \theta \sin \phi, w_U = \cos \theta \quad (6)$$

with $0 \leq \theta, \phi \leq \frac{\pi}{2}$. For any given LUT, and for any given tuple of number of included features

$(*_n_D, *_n_L, *_n_U)$, the differential impact of different categories onto the result is reflected in assigning different weights to categories. This can be seen as a fine-tuning of the non-weighted method to clarify the contribution of different categories to the total outcome. Finding optimal weights amounts to finding optimal θ, ϕ . This was implemented in this study using grid search by choosing the best combination of weights resulting from setting θ_i, ϕ_j to any point within the search grid $\theta_\alpha = \alpha\Delta\theta$ and $\phi_\alpha = \alpha\Delta\phi$ with $0 \leq \alpha \leq 10$ and $\Delta\theta = \Delta\phi = 0.05\pi$ (i.e. an 11×11 search grid).

7.4 Detailed Methodology for Model Application for Mitigation Potential Estimation

Mitigation potentials associated with the $*_n_U$ U-features over UAs (LUT 13) may be estimated for each

U-feature $*_f_k$ within $F(*_n_U) = \{*_f_k\}_{k=1}^{*_n_U}$ by in- or decreasing the testing data of that feature by $\uparrow\Delta_k$ or $\downarrow\Delta_k$, respectively, from its unvaried value where $\Delta_k = 0$ is assumed. The effect of altering U-feature

$*f_k$ may then be measured by fitting the pertaining model on the unvaried feature data and testing on the varied feature that. The method allows both to alter single U-features, or several simultaneously.

The change in the target value $\Delta\hat{T}_i$ for model i and target T — either T2 or TSK — is then estimated as the difference between average predictions from non-varied and varied U-features. For this, the predictions from the non-varied distribution $\hat{T}(\mathcal{N}_{i,\epsilon_1=200})$ and the varied distribution $\hat{T}(\mathcal{N}_{i,\epsilon_2=200})$ for the i -th model are used. In the ensemble of $\epsilon_2 = 200$ models, different random seeds were used to train on unvaried data and test against varied data. First, the responses are grouped by hours of the day:

$$\left\{ \left\{ \hat{T}_{i,h} \right\}_z^S \right\}_h^H = \left\{ \bigcup_j^{\epsilon_1} \left(\hat{T} \{ \mathcal{N}_{i,j} | \text{hour} = h \} \right) \right\}_h^H \quad (7)$$

$$\left\{ \left\{ \hat{T}'_{i,h} \right\}_z^S \right\}_h^H = \left\{ \bigcup_j^{\epsilon_2} \left(\hat{T} \{ \mathcal{N}_{i,j} | \text{hour} = h \} \right) \right\}_h^H \quad (8)$$

Each hourly slice $\left\{ \hat{T}_{i,h} \right\}_z^S$ and $\left\{ \hat{T}'_{i,h} \right\}_z^S$ contains S data points that result from aggregating the response over LUT 13. For any given hour h , the average response $\mu(\hat{T}_{i,h})$ or $\mu(\hat{T}'_{i,h})$ may then be computed as

$$\mu(\hat{T}_{i,h}) = \frac{1}{S} \sum_z^S \left\{ \hat{T}_{i,h} \right\}_z^S \quad (9)$$

$$\mu(\hat{T}'_{i,h}) = \frac{1}{S} \sum_z^S \left\{ \hat{T}'_{i,h} \right\}_z^S \quad (10)$$

For any given period of the day — day, night or the entire total day — the average response for that period $\mu(\hat{T}_i)$ or $\mu(\hat{T}'_i)$ can be found by averaging the hourly average responses over that period.

Supposing the period to consist of the hours $\{h_p\}_p^P$, the period response becomes

$$\mu(\hat{T}_i) = \frac{1}{P} \sum_p^P \mu \left(\hat{T}_{i,h_p} \right) \quad (11)$$

$$\mu(\widehat{T}'_i) = \frac{1}{p} \sum_p \mu(\widehat{T}'_{i,h_p}) \quad (12)$$

So that finally $\Delta\widehat{T}_i$ may be estimated:

$$\Delta\widehat{T}_i = \mu(\widehat{T}'_i) - \mu(\widehat{T}_i) \quad (13)$$

Union of the predicted responses in eqs. (7) and (8) occurs only over LUT 13 (urban- and built-up), and over the entire diurnal cycle. To obtain estimates on the uncertainty of the change in target value, $u(\Delta\widehat{T}_i)$, the standard errors associated with the entire data, $se(\widehat{T}_i)$ and $se(\widehat{T}'_i)$, are computed and added for the observed period:

$$u(\Delta\widehat{T}_i) = se(\widehat{T}_i) + se(\widehat{T}'_i) \quad (14)$$

$$se(\widehat{T}_{i,h}) = \frac{\sigma(\cup_p \{\widehat{T}_{i,h_p}\}_z^{Sp})}{\sqrt{\sum_h^H S_p}} \quad (15)$$

$$se(\widehat{T}'_{i,h}) = \frac{\sigma(\cup_p \{\widehat{T}'_{i,h_p}\}_z^{Sp})}{\sqrt{\sum_h^H S_p}} \quad (16)$$

where S_p indicates the number of data points in the hourly slice h_p . Finally, the target sensitivity

$\Delta\widehat{T}_i \delta_{*f_k}^{-1}$ towards unit change of $*f_k$, that is $\delta_{*f_k}^{-1}$, may be estimated via

$$\Delta\widehat{T}_i \delta_{*f_k}^{-1} = \frac{\partial \Delta\widehat{T}_i}{\partial *f_k} \approx \frac{\Delta\widehat{T}_i(*f_k + \uparrow\Delta_k) - \Delta\widehat{T}_i(*f_k - \downarrow\Delta_k)}{\uparrow\Delta_k - \downarrow\Delta_k} \quad (17)$$

The associated uncertainty of the gradient estimate, $u(\Delta\widehat{T}_i \delta_{*f_k}^{-1})$ is

$$u\left(\Delta\hat{T}_i \delta^{-1} \right) = \frac{u\left(\Delta\hat{T}_i(+\uparrow\Delta_k)\right)+u\left(\Delta\hat{T}_i(-\downarrow\Delta_k)\right)}{\uparrow\Delta_k-\downarrow\Delta_k} \quad (18)$$

This allows to assess the mitigation potential of $*f_k$, permitting to design mitigation strategies against UHIs based on expected temperature change associated with changes in feature $*f_k$.

7.5 Feature Inclusion Orders

Table 4: Feature-inclusion order (FIO) for the CB model

Rank	1	2	3	4	5	6	7	8	9	10
Feature	LWDNB	PBLH	CANWAT	UDROFF	SWDNB	ALBEDO	EMISS	SFROFF	V10	U10
Rank	11	12	13	14	15	16	17	18	19	20
Feature	QRAIN	TMN	ISLTYP	VAR_SSO	VAR	LU_INDEX	IVGTYP	VEGFRA	COSZEN	HGT
Rank	21	22								
Feature	PSFC	LAI								

Table 5: Feature-inclusion order (FIO) for the LB model.

LUT	Driving		Local			Urban
	Rank	Feature	Rank	Feature	Rank	Feature
1	1	COSZEN	1	LWDNB	1	ALBEDO
Evergreen	2	QRAIN	2	PBLH	2	IVGTYP
Needleleaf Forest	3	VAR	3	CANWAT	3	EMISS
	4	VAR_SSO	4	UDROFF	4	LAI
	5	HGT	5	SFROFF	5	VEGFRA
	6	ISLTYP	6	SWDNB		
			7	V10		
		8	U10			
		9	TMN			
		10	PSFC			
2	1	COSZEN	1	LWDNB	1	ALBEDO
Evergreen	2	QRAIN	2	PBLH	2	IVGTYP
Broadleaf Forest	3	VAR_SSO	3	CANWAT	3	EMISS
	4	HGT	4	SWDNB	4	LAI
	5	VAR	5	PSFC	5	VEGFRA
	6	ISLTYP	6	UDROFF		
			7	TMN		
			8	SFROFF		
		9	U10			
		10	V10			
4	1	COSZEN	1	LWDNB	1	EMISS
Deciduous	2	QRAIN	2	PBLH	2	ALBEDO
Broadleaf Forest	3	VAR_SSO	3	CANWAT	3	IVGTYP
	4	HGT	4	UDROFF	4	VEGFRA
	5	VAR	5	SFROFF	5	LAI
	6	ISLTYP	6	SWDNB		
			7	V10		
			8	U10		
		9	PSFC			
		10	TMN			
5	1	COSZEN	1	PBLH	1	EMISS
Mixed Forests	2	QRAIN	2	LWDNB	2	ALBEDO
	3	VAR_SSO	3	CANWAT	3	IVGTYP
	4	HGT	4	UDROFF	4	VEGFRA

	5	VAR	5	SFROFF	5	LAI
	6	ISLTYP	6	SWDNB		
			7	V10		
			8	PSFC		
			9	U10		
			10	TMN		
7	1	COSZEN	1	LWDNB	1	ALBEDO
Open Shrublands	2	QRAIN	2	PBLH	2	EMISS
	3	HGT	3	CANWAT	3	IVGTYP
	4	VAR_SSO	4	UDROFF	4	VEGFRA
	5	VAR	5	SFROFF	5	LAI
	6	ISLTYP	6	SWDNB		
			7	U10		
			8	V10		
			9	TMN		
			10	PSFC		
8	1	COSZEN	1	LWDNB	1	ALBEDO
Woody Savannas	2	QRAIN	2	SFROFF	2	EMISS
	3	HGT	3	CANWAT	3	IVGTYP
	4	VAR	4	PBLH	4	LAI
	5	VAR_SSO	5	SWDNB	5	VEGFRA
	6	ISLTYP	6	U10		
			7	TMN		
			8	UDROFF		
			9	V10		
			10	PSFC		
10	1	QRAIN	1	LWDNB	1	LAI
Grasslands	2	COSZEN	2	PBLH	2	ALBEDO
	3	HGT	3	CANWAT	3	EMISS
	4	VAR_SSO	4	UDROFF	4	IVGTYP
	5	VAR	5	SFROFF	5	VEGFRA
	6	ISLTYP	6	SWDNB		
			7	V10		
			8	U10		
			9	TMN		
			10	PSFC		
11	1	COSZEN	1	SWDNB	1	ALBEDO
Permanent Wetlands	2	QRAIN	2	CANWAT	2	IVGTYP
	3	HGT	3	SFROFF	3	LAI
	4	VAR	4	LWDNB	4	EMISS
	5	VAR_SSO	5	PBLH	5	VEGFRA
	6	ISLTYP	6	UDROFF		
			7	TMN		
			8	V10		
			9	U10		
			10	PSFC		
12	1	COSZEN	1	SWDNB	1	EMISS
Croplands	2	QRAIN	2	PBLH	2	ALBEDO
	3	HGT	3	CANWAT	3	IVGTYP
	4	VAR_SSO	4	UDROFF	4	LAI
	5	VAR	5	PSFC	5	VEGFRA
	6	ISLTYP	6	LWDNB		
			7	SFROFF		
			8	U10		
			9	V10		
			10	TMN		
13	1	QRAIN	1	SWDNB	1	EMISS
Urban and Built-Up	2	COSZEN	2	PBLH	2	ALBEDO
	3	HGT	3	PSFC	3	LAI
	4	VAR_SSO	4	CANWAT	4	IVGTYP
	5	VAR	5	UDROFF	5	VEGFRA
	6	ISLTYP	6	LWDNB		
			7	U10		
			8	SFROFF		
			9	V10		
			10	TMN		
14	1	COSZEN	1	LWDNB	1	ALBEDO
Cropland/Natural Vegetation Mosaic	2	QRAIN	2	PBLH	2	EMISS
	3	HGT	3	CANWAT	3	IVGTYP
	4	VAR_SSO	4	UDROFF	4	VEGFRA
	5	VAR	5	SFROFF	5	LAI
	6	ISLTYP	6	SWDNB		
			7	V10		
			8	U10		
			9	PSFC		

7.6 Additional Figures

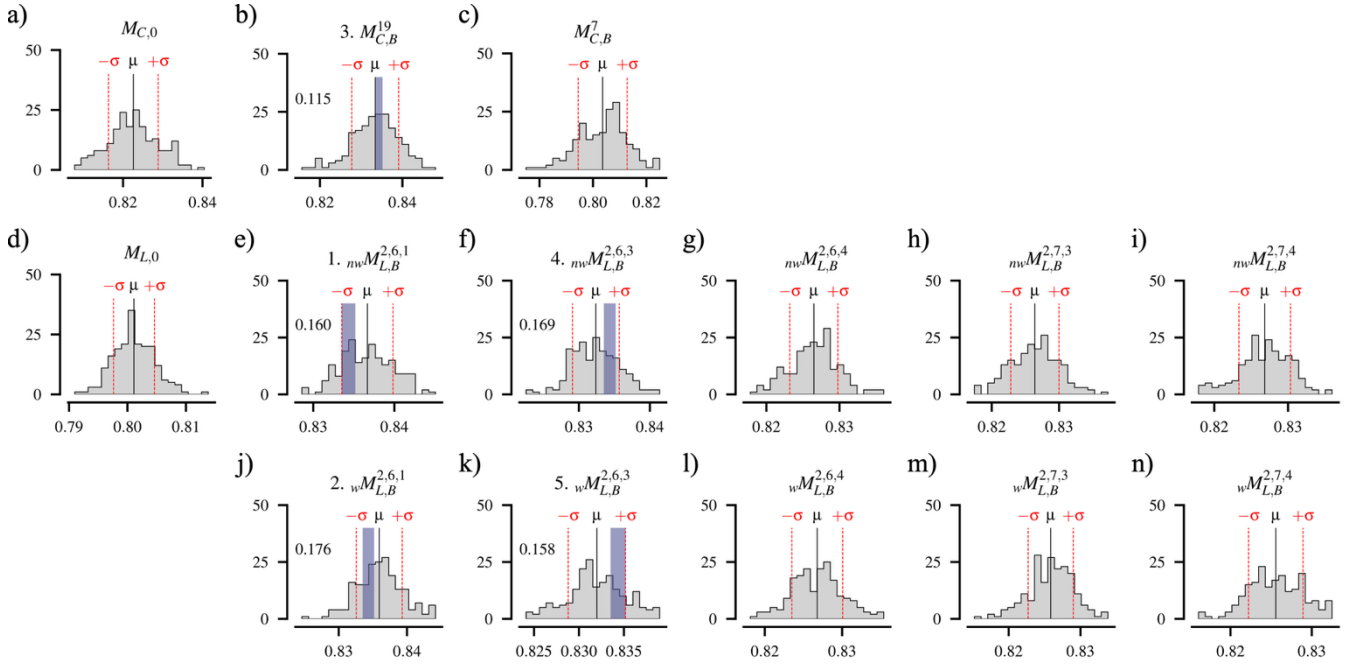


Figure 8: **a-n:** Histograms of the model accuracy distributions ($R_{\text{avg}}^2\{\mathcal{N}_{\epsilon_1=200}\}$) for all models considered. The five “top” models are indicated in the plot titles with performance ranks 1-5 marked in the respective titles. These “top” models also show a blue band that indicates the overlap in $0.8335 \leq R_{\text{avg}}^2\{\mathcal{N}_{\epsilon_1=200}\} \leq 0.8352$ shown established in sec. 3.2. The plots where the overlapping region is indicated also show the probability of finding an accuracy score within the overlap when fitting a normal distribution probability density on the pertaining histograms. **a-c:** CB models. **d-n:** LB models.

Figure 7 shows the accuracy distributions of all models considered. The “top” models are indicated (fig. 7e shows best model, indicated by “1” in the title, followed by fig. 7j, indicated by “2” in the title, and so on). Note that “top” models indicate also a probability of observing a score within the overlap, indicated as a blue ribbon. These probabilities range between 11.5% (fig. 7b) and 17.6% (fig. 7j).

8 References

- Andraju, P., Kanth, A.L., Kumari, K.V., Vijaya Bhaskara Rao, S., 2019. Performance Optimization of Operational WRF Model Configured for Indian Monsoon Region. *Earth Syst Environ* 3, 231–239. <https://doi.org/10.1007/s41748-019-00092-2>
- Aquino-Martínez, L.P., Ortega-Guerrero, B., Quintanar, A.I., Díaz-Esteban, Y., 2025. Synoptic patterns and heatwaves: Intensifying urban heat islands in the Mexico Basin. *Urban Climate* 59, 102318. <https://doi.org/10.1016/j.uclim.2025.102318>
- Benjamin, D.J., Berger, J.O., Johannesson, M., Nosek, B.A., Wagenmakers, E.-J., Berk, R., Bollen, K.A., Brembs, B., Brown, L., Camerer, C., Cesarini, D., Chambers, C.D., Clyde, M., Cook, T.D., De Boeck, P., Dienes, Z., Dreber, A., Easwaran, K., Efferson, C., Fehr, E., Fidler, F., Field, A.P.,

- Forster, M., George, E.I., Gonzalez, R., Goodman, S., Green, E., Green, D.P., Greenwald, A.G., Hadfield, J.D., Hedges, L.V., Held, L., Hua Ho, T., Hoijsink, H., Hruschka, D.J., Imai, K., Imbens, G., Ioannidis, J.P.A., Jeon, M., Jones, J.H., Kirchler, M., Laibson, D., List, J., Little, R., Lupia, A., Machery, E., Maxwell, S.E., McCarthy, M., Moore, D.A., Morgan, S.L., Munafó, M., Nakagawa, S., Nyhan, B., Parker, T.H., Pericchi, L., Perugini, M., Rouder, J., Rousseau, J., Savalei, V., Schönbrodt, F.D., Sellke, T., Sinclair, B., Tingley, D., Van Zandt, T., Vazire, S., Watts, D.J., Winship, C., Wolpert, R.L., Xie, Y., Young, C., Zinman, J., Johnson, V.E., 2018. Redefine statistical significance. *Nat Hum Behav* 2, 6–10. <https://doi.org/10.1038/s41562-017-0189-z>
- Boned Fustel, P., Cuesta Peredo, C., Boned-Ombuena, A., Carreiro, G., Fustel Rodríguez, M., 2021. Climate change and the city: analysis of the urban heat island effect on mortality in Valencia, Spain. *European Journal of Public Health* 31, ckab164.633. <https://doi.org/10.1093/eurpub/ckab164.633>
- Cai, J., Luo, J., Wang, S., Yang, S., 2018. Feature selection in machine learning: A new perspective. *Neurocomputing* 300, 70–79. <https://doi.org/10.1016/j.neucom.2017.11.077>
- Canton, J., Dipankar, A., 2024. Climatological analysis of urban heat island effects in Swiss cities. *International Journal of Climatology* 44, 1549–1565. <https://doi.org/10.1002/joc.8398>
- Carmeliet, J., Derome, D., 2024. How to beat the heat in cities through urban climate modelling. *Nat Rev Phys* 6, 2–3. <https://doi.org/10.1038/s42254-023-00673-1>
- Chen, F., Yang, X., Zhu, W., 2014. WRF simulations of urban heat island under hot-weather synoptic conditions: The case study of Hangzhou City, China. *Atmospheric Research* 138, 364–377. <https://doi.org/10.1016/j.atmosres.2013.12.005>
- Chen, T., Guestrin, C., 2016. XGBoost: A Scalable Tree Boosting System, in: *Proceedings of the 22nd ACM SIGKDD International Conference on Knowledge Discovery and Data Mining, KDD '16*. Association for Computing Machinery, New York, NY, USA, pp. 785–794. <https://doi.org/10.1145/2939672.2939785>
- Cui, Y.Y., Foy, B. de, 2012. Seasonal Variations of the Urban Heat Island at the Surface and the Near-Surface and Reductions due to Urban Vegetation in Mexico City. *Journal of Applied Meteorology and Climatology* 51, 855–868. <https://doi.org/10.1175/JAMC-D-11-0104.1>
- Ebi, K.L., Capon, A., Berry, P., Broderick, C., Dear, R. de, Havenith, G., Honda, Y., Kovats, R.S., Ma, W., Malik, A., Morris, N.B., Nybo, L., Seneviratne, S.I., Vanos, J., Jay, O., 2021. Hot weather and heat extremes: health risks. *The Lancet* 398, 698–708. [https://doi.org/10.1016/S0140-6736\(21\)01208-3](https://doi.org/10.1016/S0140-6736(21)01208-3)
- Garzón, J., Molina, I., Velasco, J., Calabia, A., 2021. A Remote Sensing Approach for Surface Urban Heat Island Modeling in a Tropical Colombian City Using Regression Analysis and Machine Learning Algorithms. *Remote Sensing* 13, 4256. <https://doi.org/10.3390/rs13214256>
- Georgescu, M., Morefield, P.E., Bierwagen, B.G., Weaver, C.P., 2014. Urban adaptation can roll back warming of emerging megapolitan regions. *Proceedings of the National Academy of Sciences* 111, 2909–2914. <https://doi.org/10.1073/pnas.1322280111>
- Giannaros, C., Nenes, A., Giannaros, T.M., Kourtidis, K., Melas, D., 2018. A comprehensive approach for the simulation of the Urban Heat Island effect with the WRF/SLUCM modeling system: The case of Athens (Greece). *Atmospheric Research* 201, 86–101. <https://doi.org/10.1016/j.atmosres.2017.10.015>
- Gudmundsson, L., Seneviratne, S.I., 2015. Towards observation-based gridded runoff estimates for Europe. *Hydrology and Earth System Sciences* 19, 2859–2879. <https://doi.org/10.5194/hess-19-2859-2015>
- Hassan, T., Zhang, J., Prodhan, F.A., Pangali Sharma, T.P., Bashir, B., 2021. Surface Urban Heat Islands Dynamics in Response to LULC and Vegetation across South Asia (2000–2019). *Remote Sensing* 13, 3177. <https://doi.org/10.3390/rs13163177>

- Heaviside, C., Macintyre, H., Vardoulakis, S., 2017. The Urban Heat Island: Implications for Health in a Changing Environment. *Curr Envir Health Rpt* 4, 296–305. <https://doi.org/10.1007/s40572-017-0150-3>
- Hua, L., Zhang, X., Nie, Q., Sun, F., Tang, L., 2020. The Impacts of the Expansion of Urban Impervious Surfaces on Urban Heat Islands in a Coastal City in China. *Sustainability* 12, 475. <https://doi.org/10.3390/su12020475>
- Intergovernmental Panel On Climate Change (IPCC), 2023. *Climate Change 2021 – The Physical Science Basis: Working Group I Contribution to the Sixth Assessment Report of the Intergovernmental Panel on Climate Change*, 1st ed. Cambridge University Press. <https://doi.org/10.1017/9781009157896>
- Keith, L., Gabbe, C.J., Schmidt, E., 2023. Urban heat governance: examining the role of urban planning. *Journal of Environmental Policy & Planning* 25, 642–662. <https://doi.org/10.1080/1523908X.2023.2244446>
- Kim, T.K., Park, J.H., 2019. More about the basic assumptions of t-test: normality and sample size. *Korean J Anesthesiol* 72, 331–335. <https://doi.org/10.4097/kja.d.18.00292>
- Kong, J., Zhao, Y., Strebel, D., Gao, K., Carmeliet, J., Lei, C., 2023. Understanding the impact of heatwave on urban heat in greater Sydney: Temporal surface energy budget change with land types. *Science of The Total Environment* 903, 166374. <https://doi.org/10.1016/j.scitotenv.2023.166374>
- Lean, H.W., Theeuwes, N.E., Baldauf, M., Barkmeijer, J., Bessardon, G., Blunn, L., Bojarova, J., Boutle, I.A., Clark, P.A., Demuzere, M., Dueben, P., Frogner, I.-L., de Haan, S., Harrison, D., Heerwaarden, C. van, Honnert, R., Lock, A., Marsigli, C., Masson, V., McCabe, A., Reeuwijk, M. van, Roberts, N., Siebesma, P., Smolíková, P., Yang, X., 2024. The hectometric modelling challenge: Gaps in the current state of the art and ways forward towards the implementation of 100-m scale weather and climate models. *Quarterly Journal of the Royal Meteorological Society* 150, 4671–4708. <https://doi.org/10.1002/qj.4858>
- Li, D., Bou-Zeid, E., 2013. Synergistic Interactions between Urban Heat Islands and Heat Waves: The Impact in Cities Is Larger than the Sum of Its Parts. *Journal of Applied Meteorology and Climatology* 52, 2051–2064. <https://doi.org/10.1175/JAMC-D-13-02.1>
- Li, H., Zhou, Y., Wang, X., Zhou, X., Zhang, H., Sodoudi, S., 2019. Quantifying urban heat island intensity and its physical mechanism using WRF/UCM. *Science of The Total Environment* 650, 3110–3119. <https://doi.org/10.1016/j.scitotenv.2018.10.025>
- Li, X.-X., Norford, L.K., 2016. Evaluation of cool roof and vegetations in mitigating urban heat island in a tropical city, Singapore. *Urban Climate* 16, 59–74. <https://doi.org/10.1016/j.uclim.2015.12.002>
- Liu, B., Guo, X., Jiang, J., 2023. How Urban Morphology Relates to the Urban Heat Island Effect: A Multi-Indicator Study. *Sustainability* 15, 10787. <https://doi.org/10.3390/su151410787>
- McCarty, D., Lee, J., Kim, H.W., 2021. Machine Learning Simulation of Land Cover Impact on Surface Urban Heat Island Surrounding Park Areas. *Sustainability* 13, 12678. <https://doi.org/10.3390/su132212678>
- Mohammad, P., Goswami, A., Chauhan, S., Nayak, S., 2022. Machine learning algorithm based prediction of land use land cover and land surface temperature changes to characterize the surface urban heat island phenomena over Ahmedabad city, India. *Urban Climate* 42, 101116. <https://doi.org/10.1016/j.uclim.2022.101116>
- Oke, T.R., 1982. The energetic basis of the urban heat island. *Quart J Royal Meteor Soc* 108, 1–24. <https://doi.org/10.1002/qj.49710845502>
- Phelan, P.E., Kaloush, K., Miner, M., Golden, J., Phelan, B., Iii, H.S., Taylor, R.A., 2015. Urban Heat Island: Mechanisms, Implications, and Possible Remedies. *Annual Review of Environment and Resources* 40, 285–307. <https://doi.org/10.1146/annurev-environ-102014-021155>

- Raschka, S., Mirjalili, V., 2019. Python Machine Learning: Machine Learning and Deep Learning with Python, Scikit-Learn, and TensorFlow 2. Packt Publishing, Limited, Birmingham, UNITED KINGDOM.
- Ren, J., Shi, K., Li, Z., Kong, X., Zhou, H., 2023. A Review on the Impacts of Urban Heat Islands on Outdoor Thermal Comfort. *Buildings* 13, 1368. <https://doi.org/10.3390/buildings13061368>
- Skamarock, C., Klemp, B., Dudhia, J., Gill, O., Liu, Z., Berner, J., Wang, W., Powers, G., Duda, G., Barker, D., Huang, X., 2021. A Description of the Advanced Research WRF Model Version 4.3. <https://doi.org/10.5065/1dfh-6p97>
- Tanoori, G., Soltani, A., Modiri, A., 2024. Machine Learning for Urban Heat Island (UHI) Analysis: Predicting Land Surface Temperature (LST) in Urban Environments. *Urban Climate* 55, 101962. <https://doi.org/10.1016/j.uclim.2024.101962>
- United Nations Organisation, 2019. World Urbanization Prospects: The 2018 Revision (No. ST/ESA/SER.A/420). United Nations, Department of Economic and Social Affairs, Population Division, New York.
- Vahmani, P., Ban-Weiss, G.A., 2016. Impact of remotely sensed albedo and vegetation fraction on simulation of urban climate in WRF-urban canopy model: A case study of the urban heat island in Los Angeles. *Journal of Geophysical Research: Atmospheres* 121, 1511–1531. <https://doi.org/10.1002/2015JD023718>
- Varentsov, M., Konstantinov, P., Baklanov, A., Esau, I., Miles, V., Davy, R., 2018. Anthropogenic and natural drivers of a strong winter urban heat island in a typical Arctic city. *Atmospheric Chemistry and Physics* 18, 17573–17587. <https://doi.org/10.5194/acp-18-17573-2018>
- Verein Klimaseniorinnen Schweiz and Others v. Switzerland, 2024.
- Wang, H., Yang, J., Chen, G., Ren, C., Zhang, J., 2023. Machine learning applications on air temperature prediction in the urban canopy layer: A critical review of 2011–2022. *Urban Climate* 49, 101499. <https://doi.org/10.1016/j.uclim.2023.101499>
- Wang, J., Balaprakash, P., Kotamarthi, R., 2019. Fast domain-aware neural network emulation of a planetary boundary layer parameterization in a numerical weather forecast model. *Geoscientific Model Development* 12, 4261–4274. <https://doi.org/10.5194/gmd-12-4261-2019>
- Wang, R., 2023. Application of Machine Learning in Prediction of Urban Heat Island, in: Gao, W. (Ed.), *Digital Analysis of Urban Structure and Its Environment Implication*. Springer Nature, Singapore, pp. 171–206. https://doi.org/10.1007/978-981-19-6641-5_7
- Ward, K., Lauf, S., Kleinschmit, B., Endlicher, W., 2016. Heat waves and urban heat islands in Europe: A review of relevant drivers. *Science of The Total Environment* 569–570, 527–539. <https://doi.org/10.1016/j.scitotenv.2016.06.119>
- Yang, J., Zhou, M., Ren, Z., Li, M., Wang, B., Liu, D.L., Ou, C.-Q., Yin, P., Sun, J., Tong, S., Wang, H., Zhang, C., Wang, J., Guo, Y., Liu, Q., 2021. Projecting heat-related excess mortality under climate change scenarios in China. *Nat Commun* 12, 1039. <https://doi.org/10.1038/s41467-021-21305-1>
- Zhao, L., Lee, X., Smith, R.B., Oleson, K., 2014. Strong contributions of local background climate to urban heat islands. *Nature* 511, 216–219. <https://doi.org/10.1038/nature13462>
- Zhong, X., Ma, Z., Yao, Y., Xu, L., Wu, Y., Wang, Z., 2023. WRF–ML v1.0: a bridge between WRF v4.3 and machine learning parameterizations and its application to atmospheric radiative transfer. *Geoscientific Model Development* 16, 199–209. <https://doi.org/10.5194/gmd-16-199-2023>